**Astronomy
&
Astrophysics**

Extending the supernova Hubble diagram to *z* ∼ 1.5 with the *Euclid* space mission

P. Astier[1], C. Balland[1], M. Brescia[2], E. Cappellaro[3], R. G. Carlberg[4], S. Cavuoti[5], M. Della Valle[2,6], E. Gangler[7], A. Goobar[8], J. Guy[1], D. Hardin[1], I. M. Hook[9,10], R. Kessler[11,12], A. Kim[13], E. Linder[14], G. Longo[5], K. Maguire[9,15], F. Mannucci[16], S. Mattila[17], R. Nichol[18], R. Pain[1], N. Regnault[1], S. Spiro[9], M. Sullivan[19], C. Tao[20,21], M. Turatto[3], X. F. Wang[21], and W. M. Wood-Vasey[22]

[1] LPNHE, CNRS/IN2P3, Université Pierre et Marie Curie Paris 6, Université Denis Diderot Paris 7, 4 place Jussieu, 75252 Paris Cedex 5, France
e-mail: pierre.astier@in2p3.fr
[2] INAF, Capodimonte Astronomical Observatory, via Moiariello 16, 80131 Naples, Italy
[3] INAF–Osservatorio Astronomico di Padova, Vicolo dell'Osservatorio 5, 35122 Padova, Italy
[4] Department of Astronomy and Astrophysics, University of Toronto, 50 St. George Street, Toronto ON M5S 3H4, Canada
[5] Dept. of Physics, University Federico II, via Cinthia, 80126 Naples, Italy
[6] International Center for Relativistic Astrophysics, Piazza Repubblica, 10, 65122 Pescara, Italy
[7] Clermont Université, Université Blaise Pascal, CNRS/IN2P3, Laboratoire de Physique Corpusculaire, BP 10448, 63000 Clermont-Ferrand, France
[8] Albanova University Center, Department of Physics, Stockholm University, Roslagstullsbacken 21, 106 91 Stockholm, Sweden
[9] Department of Physics (Astrophysics), University of Oxford, DWB, Keble Road, Oxford OX1 3RH, UK
[10] INAF–Osservatorio Astronomico di Roma, via Frascati 33, 00040 Monteporzio (RM), Italy
[11] Department of Astronomy and Astrophysics, University of Chicago, 5640 South Ellis Avenue, Chicago, IL 60637, USA
[12] Kavli Institute for Cosmological Physics, University of Chicago, 5640 South Ellis Avenue Chicago, IL 60637, USA
[13] LBNL, 1 Cyclotron Rd, Berkeley CA 94720, USA
[14] University of California Berkeley, CA 94720 USA
[15] European Southern Observatory, Karl-Schwarzschild-Str. 2, 85748 Garching bei München, Germany
[16] INAF, Osservatorio Astrofisico di Arcetri, Largo E. Fermi 5, 50125 Firenze, Italy
[17] Finnish Centre for Astronomy with ESO (FINCA), University of Turku, Väisäläntie 20, 21500 Piikkiö, Finland
[18] Institute of Cosmology & Gravitation, University of Portsmouth, Portsmouth PO1 3FX, UK
[19] School of Physics and Astronomy, University of Southampton, Southampton, SO17 1BJ, UK
[20] CPPM, Université Aix-Marseille, CNRS/IN2P3, Case 907, 13288 Marseille Cedex 9, France
[21] Tsinghua center for astrophysics, Physics department, Tsinghua University, 100084 Beijing, PR China
[22] PITT PACC, Department of Physics and Astronomy, University of Pittsburgh, Pittsburgh PA 15260, USA

ABSTRACT

We forecast dark energy constraints that could be obtained from a new large sample of Type Ia supernovae where those at high redshift are acquired with the *Euclid* space mission. We simulate a three-prong SN survey: a $z < 0.35$ nearby sample (8000 SNe), a $0.2 < z < 0.95$ intermediate sample (8800 SNe), and a $0.75 < z < 1.55$ high-*z* sample (1700 SNe). The nearby and intermediate surveys are assumed to be conducted from the ground, while the high-*z* is a joint ground- and space-based survey. This latter survey, the "Dark Energy Supernova Infra-Red Experiment" (DESIRE), is designed to fit within 6 months of *Euclid* observing time, with a dedicated observing programme. We simulate the SN events as they would be observed in rolling-search mode by the various instruments, and derive the quality of expected cosmological constraints. We account for known systematic uncertainties, in particular calibration uncertainties including their contribution through the training of the supernova model used to fit the supernovae light curves. Using conservative assumptions and a 1D geometric *Planck* prior, we find that the ensemble of surveys would yield competitive constraints: a constant equation of state parameter can be constrained to $\sigma(w) = 0.022$, and a Dark Energy Task Force figure of merit of 203 is found for a two-parameter equation of state. Our simulations thus indicate that *Euclid* can bring a significant contribution to a purely geometrical cosmology constraint by extending a high-quality SN Ia Hubble diagram to $z \sim 1.5$. We also present other science topics enabled by the DESIRE *Euclid* observations.

Key words. cosmological parameters – dark energy

1. Introduction

Measuring distances to supernovae Ia (SNe Ia) at $z \sim 0.5$ allowed two teams (Riess et al. 1998; Schmidt et al. 1998; Perlmutter et al. 1999) to independently discover that the expansion of the Universe is now accelerating. The cause of this acceleration at late times is still unknown and has been attributed to a new component in the Universe admixture: dark energy. One can describe the acceleration at late times through the equation of state of dark energy w (namely how its density evolves with redshift and cosmic time), and the current results are compatible with a static density, i.e. a cosmological constant

(e.g. Betoule et al. 2014). Measuring precisely this equation of state constitutes a crucial step towards understanding the nature of dark energy (Albrecht et al. 2006; Peacock et al. 2006). Since the discovery of acceleration, we have narrowed the allowed region of parameter space, from SNe[1] (e.g. Riess et al. 2004; Astier et al. 2006; Riess et al. 2007; Wood-Vasey et al. 2007; Kessler et al. 2009; Conley et al. 2011; Sullivan et al. 2011; Planck Collaboration XVI 2014; Betoule et al. 2014; Sako et al. 2014), and also with other probes (e.g. Schrabback et al. 2010; Blake et al. 2011; Riess et al. 2011; Burenin & Vikhlinin 2012; Planck Collaboration XVI 2014; Amati & Valle 2013). Investigating the uncertainties of w measurements reveals that distances to SNe are leading precision constraints. The current constraints on a constant equation of state from a joint fit of a flat w cold dark matter (wCDM) cosmological model to the SN Hubble diagram and *Planck* cosmic microwave background (CMB) measurements yields $w = -1.018 \pm 0.057$(stat + sys) (Betoule et al. 2014).

However, it is important to realise that in the quest for stricter dark energy constraints, one should rely on several probes: different probes face different parameter degeneracies and efficiently complement each other; different probes are also subject to different systematic uncertainties, and a cross-check is obviously in order for these delicate measurements. Both arguments are developed in detail in Albrecht et al. (2006); Peacock et al. (2006).

When one constrains cosmological parameters from distance data, increasing the redshift span of the data efficiently improves the quality of cosmological constraints, and SN surveys are hence targeting the highest possible redshifts. Cosmological constraints from SNe derive from comparing event brightnesses at different redshifts. For precision cosmology, one should aim at comparing similar restframe wavelength regions at all redshifts, so that the comparison does not strongly rely on a SN model. When aiming at higher and higher redshifts, ground-based SN surveys face two serious limitations related to the atmosphere: at wavelengths redder than ~800 nm, the atmosphere glow rises rapidly in intensity; this glow goes with large and time-variable atmospheric absorption which makes precision photometry through the atmosphere above 1 μm very difficult.

Cosmological constraints from SN distances are currently dominated by distances measured in the visible, mainly at $z \lesssim 1$, (e.g. Conley et al. 2011; Scolnic et al. 2014a; Betoule et al. 2014). The current sample of SN distances at $z > 1$ is dominated by events measured with NIR instruments (NICMOS and WFC3) on the HST (Riess et al. 2007; Suzuki et al. 2012; Rodney et al. 2012; Rubin et al. 2013) and amounts to less than 40 such events. These NIR instruments have a small field of view compared to current ground-based CCD-mosaics. Extending the Hubble diagram of supernovae at $z \gtrsim 1$ with statistics matching forthcoming ground-based samples at $z \lesssim 1$ requires NIR wide-field imaging from space.

Euclid is an ESA M-class space mission, adopted in June 2012, which aims at characterising dark energy, from two main probes (Laureijs et al. 2011): the spatial correlations of weak shear, and the 3D correlation function of galaxies. The latter allows one to measure in particular the evolution of the expansion rate of the Universe by tracking the BAO peak as a function of redshift, while the study of the shear as a function of redshift constrains both the expansion rate evolution and the growth rate of structures. The growth rate of structures, and its

evolution with redshift can also be probed by extracting redshift space distortions from the envisioned 3D galaxy redshift survey. Measuring both the expansion history and the growth rate evolution with redshift provides a new test of general relativity on large scales because this theory predicts a specific relation between these two aspects. Alternative theories of gravity, which might be invoked instead of dark energy, predict in general a different relation between growth of structures and expansion history (e.g. Lue et al. 2004; Linder 2005; Bean et al. 2007; Bernardeau & Brax 2011; Amendola et al. 2013, and references therein).

Euclid will be equiped with a wide-field NIR imager and is hence well suited to host a high-statistics high-redshift supernova programme, aimed at extending the ground-based Hubble diagram beyond $z \sim 1$. This paper proposes such a SN survey and evaluates the cosmological constraints it could deliver in association with measurements of distances to SNe at lower redshifts with ground-based instruments. An earlier paper (Astier et al. 2011, A11 thereafter) aimed at designing a standalone space-based SN survey and suggested a different route: it assumed that a *Euclid*-like mission could be equipped with a filter wheel on its visible imager, which is no longer a plausible possibility within the adopted mission constraints. However, some arguments developed in A11 still apply to the work presented here and we will refer to this earlier study when applicable.

We present here a SN survey which addresses systematic concerns and delivers valuable leverage on dark energy. The plan of this paper is as follows: we will first discuss the requirements of SN Ia surveys for high-quality distances (Sect. 2). We then describe the salient points of our SN and instrument simulators (Sect. 3). The proposed surveys are described in Sect. 4, and the assumptions regarding redshifts and typing in Sect. 5. The forecast methodology and the associated Fisher matrix are the subjects of Sect. 6. Our results are presented in Sect. 7, and we explore alternatives to the baseline surveys in Sect. 7.1. In Sect. 8, we compare our findings to forecasts for the SN survey projects within DES and WFIRST. We discuss issues related to astrophysics of supernovae and their host galaxies in Sect. 9. The data set we propose to collect with *Euclid* allows a wealth of other science studies, and we present a sample of those in Sect. 10. We summarise in Sect. 11.

2. Requirements for the supernova survey

Distances to SNe Ia rely on the comparison of supernova fluxes at different redshifts. The evolution of distances (up to a global multiplicative constant) with redshift encodes the expansion history of the Universe. We will now discuss various aspects of the SN survey design intended to limit the impact of systematic uncertainties.

One can summarise the current impact of systematic uncertainties on SN cosmology (Guy et al. 2010; Conley et al. 2011; Sullivan et al. 2011, also known as SNLS3): the photometric calibration uncertainties dominate by far over other systematics, and contribute to the equation of state uncertainty by about as much as statistics (see e.g. Table 7 from Conley et al. 2011). For the latest SN+*Planck* results (Betoule et al. 2014), the calibration uncertainties increase $\sigma(w)$ from 0.044 to 0.057. There are, however, ways to reduce the impact of calibration uncertainties both in the survey design, and in the calibration scheme. Regarding the latter, adding new calibration paths (Betoule et al. 2013) to the classical path via the Landolt catalogue (e.g. Regnault et al. 2009) already reduced significantly the calibration uncertainty. Half of the current calibration uncertainty is due to

---

[1] In this paper, SN and SNe mostly refer to Type Ia supernovae rather than supernovae in a more general sense.
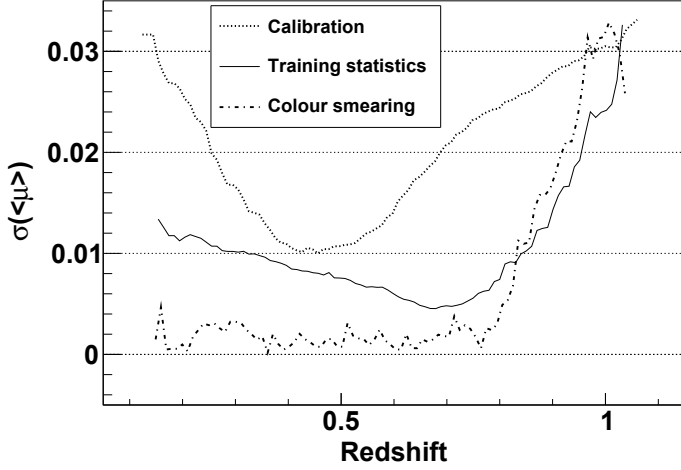
Fig. 1. Contribution of various sources to correlated uncertainties, averaged over sliding $\Delta z = 0.2$ bins for the SNLS3 analysis (data from Guy et al. 2010). "Colour smearing" refers to the effect of uncertainties of the band-dependent residual scatter model (see Sect. 3.3). The steep increase at high redshift of this contribution and of that from SN model training statistics are both due to those events being measured in bands bluer in the rest-frame than the lower redshift events. We note that these two contributions are indeed going down with sample size.

primary calibrators which is expected to decrease in the future. The SNLS3 compilation is dominated at high redshift by the SNLS sample, measured in the visible from the ground using a camera that has limited sensitivity in its reddest band (i.e. the *z*-band). This specific feature affects the precision of SNLS distances at $z \gtrsim 0.8$, as discussed below. We discuss now how the SN survey design can mitigate calibration uncertainties.

2.1. Wavelength coverage

If fluxes of SNe at different redshifts are measured at different *restframe* wavelengths, one has to rely on some modelling of the spectrum of SNe in order to convert relative fluxes to relative distances. Distances relying on such a model are affected by systematic and statistical uncertainties from this model, correlating all events at the same redshift. This effect is illustrated in the case of the SNLS survey by the Fig. 1, where one can see that at the high-redshift end, uncertainties unrelated to the measurement itself become important, especially because they are common to all events. Because of the low sensitivity of the imager in *z* band, these high redshift events are effectively measured in bluer restframe bands than events at lower redshifts, which makes their distances sensitive to statistical and systematic uncertainties of the SN model. This SN model always derives from a training sample and inherits all uncertainties affecting this training sample. In particular, the calibration uncertainties affecting the SN model training sample propagate to these distances to high-redshift events measured in restframe bands extending bluer than *U*. So, a strategy requiring that all events be measured in similar restframe bands reduces the impact of SN model uncertainties on distances. We propose below a quantitative implementation of this requirement.

2.2. Amplitude, colour, and distance uncertainties

The signal-to-noise ratio (S/N) of the photometric measurements affects the precision of distances, but at some point, distances will not significantly benefit from deeper exposures. We discuss here current intrinsic limitations of supernova distances as well as how measurement precision contributes to distance precision.

SNe Ia exhibit some variability both in light curve shape and colour, both correlated with brightness (e.g. Tripp & Branch 1999, and references therein) and most SN distance estimators rely in some way on these brighter-slower and brighter-bluer relations. A common way of parametrising a distance modulus $\mu \equiv 5 \log_{10}(d_L)$, accounting for these relations is

$$\mu = m_B^* + \alpha(s - 1) - \beta c - \mathcal{M}, \qquad (1)$$

where m_B^*, s, c are fitted SN-dependent parameters. m_B^* denotes the peak brightness in restframe *B* filter, *s* is a stretch factor describing the light curve width (or decline rate), and *c* is a restframe colour most often chosen as $B-V$ evaluated at peak brightness. α, β and $\mathcal{M}$ are global parameters derived from data (and subsequently marginalised over), typically by minimizing the distance scatter. They do not convey cosmological information, but rather parametrise the brighter-slower, brighter-bluer and intrinsic brightness of SNe. For each event, the m_B^*, s, c parameters are derived from a fit of a SN model to the measured light curve points, in at least two bands, if colour is to be measured. The m_B^* and *c* parameters, which mainly determine the distance precision, are derived from amplitudes of light curves in different bands, where "amplitude" refers to some brightness indicator (e.g. the peak brightness) derived from the light curve in a single band. We will now discuss the requirements on the quality of photometric measurements, and express those using amplitude precision.

The contribution of the *s* uncertainty to the μ uncertainty is sub-dominant for light curves spanning at least $\sim$30 restframe days. On the contrary, since β turns out to be larger than 1 (for $c = B - V$ restframe, $\beta_{B,V}$ is indeed measured to be above 3, see e.g. Guy et al. 2010), the *c* measurement uncertainty drives the distance measurement uncertainty. Since the observed scatter of SNe distance moduli (given by Eq. (1)) around the Hubble diagram is at best about 0.15 mag, *c* measurement uncertainties above $\sim$0.04 mag will start to contribute significantly to the distance uncertainty. Figure 2 shows that the SNLS survey is within this bound up to $z = 1$. This performance is however obtained on a sample that is effectively flux-selected by spectroscopic identification, and that relies on the *r* band to measure colour at the highest redshifts. This restframe UV region is affected by large fluctuations from event to event (Fig. 4 of Maguire et al. 2012, Fig. 8 of Guy et al. 2010). Worse, Fig. 4 of Maguire et al. (2012) may suggest an evolution with redshift of the flux at wavelengths shorter than 320 nm. So, we give up the rest-frame UV region by requiring that filters with central wavelength below 380 nm in the rest-frame are not used for distances. Amplitudes of light curves in the BVR rest-frame region measured to a precision of 0.04 mag deliver a colour precision of about 0.045 mag with two bands, and better than 0.03 mag with 3 bands. We note that measurements in the rest-frame UV, even if not used for distances, are still available for photometric identification. Measurements at $\sim$280 nm (rest frame) are available in certain redshift ranges, and can be used as a possible control of evolution of supernovae, as discussed in Sect. 9.2.

When a sizable fraction of the SN Ia population is lost at the high-redshift end of the Hubble diagram because of flux selection, one has to simulate the unobserved events to correct for the bias of the observed sample. This procedure aims at compensating for the so-called Malmquist bias, but the uncertainties of such a procedure (see e.g. Wood-Vasey et al. 2007; Kessler et al. 2009; Perrett et al. 2010; Conley et al. 2011; Kessler et al. 2013) limit the usefulness of an incomplete high redshift sample. On top of possible systematics, there is a statistical price to pay: an incomplete high redshift sample is on average bluer than the
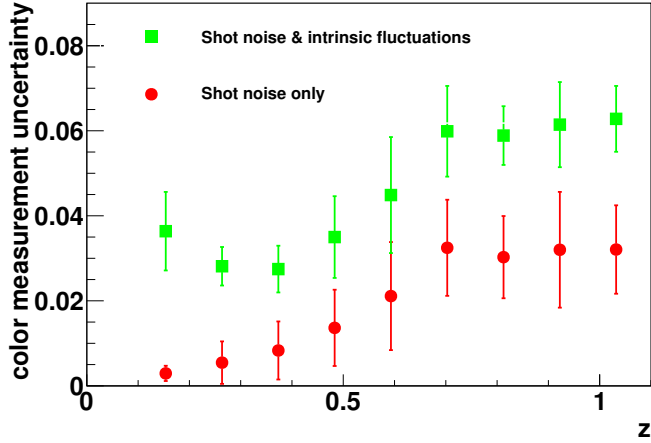
Fig. 2. Measurement uncertainty of the *c* parameter in the SNLS survey as a function of redshift, for events spectroscopically identified. Solid circles show the contribution of the source shot noise alone, and the squares include intrinsic fluctuations from event to event (also called colour smearing). At $z > 0.7$, the shot noise contribution becomes essentially constant because the colour measurement relies on bluer and bluer restframe bands, which are more and more sensitive to colour changes. This might look favourable, but accounting for intrinsic fluctuations from event to event (squares), very large in the UV, swamps this benefit. (Data obtained from fitting light curves from Guy et al. 2010.)
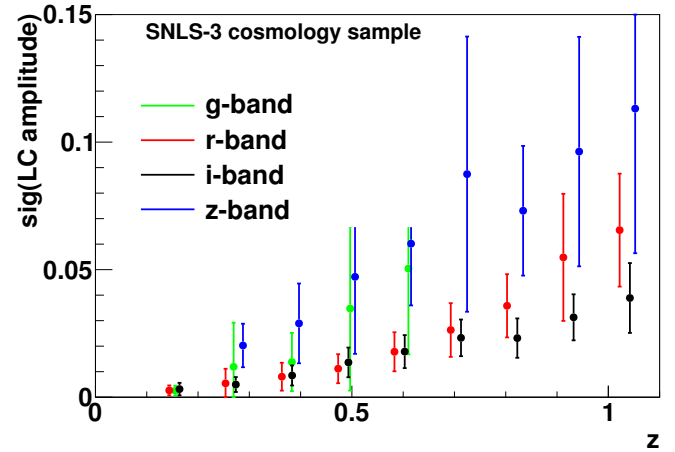

Fig. 3. Measurement uncertainties of fitted amplitudes of SNLS light curves, propagating shot noise. The *i*-band precision is below 0.03 mag up to $z = 1$, as well as the *r*-band up to $z \simeq 0.75$. SNLS observations rely on thinned CCDs with a low QE in *z*-band. This band is thus shallow and hence has a small weight in distances to high-redshift events. (Data from fitting light curves from Guy et al. 2010.)

whole population, and induces correlations between β (Eq. (1)) and cosmological parameters[2] which degrade the quality of cosmological constraints. Conversely, if the SN colour distribution of the cosmological sample is the same at all redshifts, a wrong β or even an inadequate form of the colour correction affects SNe at all redshifts in the same way, and hence does not alter the average distance-redshift relation. So, all efforts need be made to retain a very large fraction of the population at the highest redshift. Since high-redshift red SNe are very faint and thus missing from SN samples, one can eliminate the potential bias by ignoring red events at all redshifts. The analyses typically reject both blue and red events beyond 2.5 to 3σ (see e.g. Kessler et al. 2009; Conley et al. 2011) from the mean of the restframe $B - V$ distribution and the statistical cost is at the few percent level.

2.3. Light curve measurement precision requirements

We propose the following quality requirements for photometric measurements of SNe Ia aimed at deriving distances:

1. We express the quality of light curve measurements from the r.m.s uncertainty of their fitted amplitude. Our goal is to secure two bands measured to a precision of 0.04 mag and a third band to 0.06 mag. *Rationale*: this ensures a colour measured to 0.03 mag, such that the colour uncertainty is sub-dominant in the distance uncertainty. As long as measurements meet this quality, there are no detection losses, because detection and photometric measurements are carried out from the same images. By discarding events at redshifts that do not meet these quality requirements, we effectively construct redshift-limited surveys.
2. Do not use filters with central wavelength below 380 nm in the restframe. *Rationale*: SNe Ia have large dispersions in the UV, and there are indications of evolution below 330 nm.
3. Derive distances from most similar restframe regions at all redshifts. To this aim, we only consider filters with central wavelengths $380 < \lambda < 700$ nm. *Rationale:* reduce dependence on SN model and its associated systematic (e.g. calibration of the training sample) and statistical uncertainties.
4. Measure light curves over $[-10, +30]$ restframe days from maximum light. *Rationale*: measure light curve width in order to account for the brighter-slower relation, and provide light curve shape information for SN typing. Compare rise and decline rates across redshifts for evolution tests.

These requirements will be used as guidelines for the SN survey designs in Sect. 4. Figure 3 shows that the SNLS observations meet these requirements up to $z = 0.65$; they fail at higher redshifts because of the modest sensitivity in *z*-band (the CCDs of Megacam (Boulade et al. 2003) are optimised for blue wavelengths). An imager equipped with deep-depleted thick CCDs can meet our requirements up to $z \simeq 0.95$, acquiring deep enough *y*-band data, and with exposures significantly deeper than SNLS. The strategy proposed for DES in Bernstein et al. (2012) does not provide three bands redder than 380 nm at $z \gtrsim 0.68$, because it does not plan on using the low-efficiency *y* band.

Euclid hosts a visible imager, called VIS, equipped with a single broad band $500 \lesssim \lambda \lesssim 950$ nm, in order to maximise the S/N of galaxy shape measurements. Such a band corresponds to merging two to three regular broadband filters. The requirements above exclude using this band for measuring distances to SNe at $z \gtrsim 0.5$, because at higher redshifts, it includes too blue rest-frame regions. More generally, our requirement that measurements are similar across redshifts excludes an observer band much wider than the others. However, deep *Euclid* visible data of the SN hosts will be valuable for other reasons, discussed in Sect. 10.

---

[2] From the distance modulus definition (Eq. (1)), one can infer that if the average colour $\langle c \rangle$ is independent of z, the average distance modulus $\langle \mu \rangle$ does not depend on β and hence estimates of cosmological parameters and β are independent. In Kessler et al. (2013, Sect. 6.4), it is shown that the value of β influences both the evaluation of Malmquist bias and distance moduli in ways which tend to cancel each other on average. The statistical coupling between cosmological parameters and β however remains.

2.4. Cadence of the survey

In the above requirements, we have not discussed the sampling cadence along the light curves because we have expressed the depth requirement directly on the fitted light curve amplitude (point 1). If an observing cadence meets this requirement, visits twice as frequent integrating half the exposure time will not change significantly the precision of the fitted amplitude. As a baseline, we adopt in what follows a four-day cadence in the observer frame, because this is more than adequate to sample light curves of high-redshift supernovae and allows one to efficiently study faster transients. We could measure distances to SNe Ia using a somehow slower cadence, but with accordingly deeper exposures at each visit.

3. Instrument and supernova simulators

3.1. Instrument simulator

In its current design, *Euclid* is equipped with a visible and a NIR imager (Laureijs et al. 2011). The latter also has a slitless spectroscopic mode but what we will discuss here does not rely on this capability, mainly because high redshift SNe are too faint for slitless spectrocopy on *Euclid* to deliver a usable signal. We do not rely either on the visible imager for measuring distances, as mentioned above. Therefore, the SN observations we are going to discuss rely solely on the NIR *Euclid* imager.

In order to assess the cosmological performance of possible surveys, we simulate SN observations in *Euclid* and other imaging instruments. The first step is to evaluate the precision of photometric measurements. For a given SED, observing setup and observing strategy, our simulator computes the expected flux and evaluates the flux uncertainty assuming measurements are carried out using PSF photometry for a given sky background and detector-induced noise, and accounts for shot noise from the source; this calculation is described in Appendix A. For *Euclid*'s NIR imager, we use PSFs derived from full optical simulations (including diffraction) and detector characteristics[3]. These optical simulations were used to define the exposure times for NIR imaging in the *Euclid* observing plan for its core science. The most important parameters of our *Euclid* NIR imager simulator are:

- a mirror area of 9300 cm^2;
- a read-noise of 7 electrons;
- a dark current of 0.1 electrons/pixel/s;
- pixels subtend 0.3″ on a side;
- and the imager covers 0.5 deg^2 on the sky.

This NIR imager has 3 bands (named y, J and H) roughly covering the [1−2] μm interval. The overall transmission of the imager bands (accounting for all optical transmissions and quantum efficiency of the sensors) are shown in Fig. 4. The important parameters of the simulated photometry bands are provided in Table 1.

We have used the zodiacal light models in space from Leinert et al. (1998), more precisely the angular dependence from their Table 16, and the spectral dependence from their Table 19. The zodiacal light intensity depends on the ecliptic latitude because of the albedo of solar system dust, and the darkest spots are the ecliptic poles. Our Table 1 presents sky brightnesses at two ecliptic latitudes. The brightest one, S_{45} refers to 45° from the
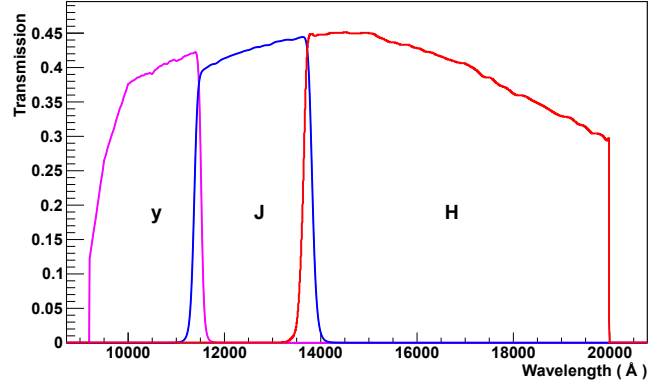
---

[3] We are in debt to R. Holmes for providing us with the PSFs, transmission curves displayed in Fig. 4 and sensor characteristics which allowed us to simulate NIR imaging with *Euclid*.

Fig. 4. Overall transmission of the 3 bands of the *Euclid* NIR imaging system, in its current design. The *H* filter red cutoff has been pushed to 2 μm compared to earlier designs. The cut-on of the y filter is determined by the dichroic that splits the beam between visible and NIR instruments.

Table 1. Characteristics of the *Euclid* bands simulated for the high-redshift survey.

Band	$\bar{\lambda}$ (nm)	S_{45} (AB/arcsec^2)	S_{15} (AB/arcsec^2)	ZP (m_{AB} for 1e$^-$/s)	NEA (arcsec^2)
y	1048	22.47	22.75	24.03	0.56
J	1263	22.44	22.72	24.08	0.61
H	1658	22.31	22.60	24.74	0.77

Notes. Columns include: central wavelength, sky brightness (in *AB* magnitudes/arcsec^2) at two separations from the ecliptic poles (45° and 15°), zero-points (for *AB* magnitudes and fluxes in e$^-$/s), and Noise Equivalent Area (NEA) of the PSF (defined by Eq. (A.1)). This is the area over which one integrates the sky background fluctuations when performing PSF photometry for faint sources, accounting for pixelisation at 0.3″/pixel. The reported NEA values were averaged over source position within the central pixel.

ecliptic pole where we assumed a zodiacal light flux density normalised to 7.54×10^{-19} erg/(cm^2 s Å arcsec^2) at 1.2 μm. With this value, our simulator derives 5σ limiting *AB* magnitudes of 24.02, 24.03, and 23.98 for three exposures of 79, 81 and 48 s in y, J and H respectively, assuming PSF photometry is carried out. These values compare very well to the limiting magnitudes of 24.00 (set by scientific requirements, see Laureijs et al. 2011) found by the instrument development team, who indeed derived the above exposure times of the "*Euclid* standard visit" that deliver this sensitivity.

Fields selected to monitor SN light curves have to be observable over long periods of time, and the *Euclid* spacecraft design imposes that they are located near the ecliptic poles. We will hence use in what follows the S_{15} sky intensities from our Table 1 which apply at 15° and closer to the ecliptic poles. Our 5σ limiting magnitudes for 3 standard *Euclid* exposures (79, 81, 48 s in y, J, H) then become 24.05, 24.07 and 24.03 in y, J and H respectively, i.e. they are improved by ∼0.04 with respect to 45° from the ecliptic poles. The improvement with decreasing sky background is modest because read noise contributes ∼60 % to the total noise of the NIR standard *Euclid* exposures.

3.2. Impact of finite reference image depth

Supernovae photometry is obtained by subtracting images without the supernova (deemed the reference images) from images

with the supernova. Since the same SN-free images are subtracted from all light curves measurements, the SN fluxes along the light curve are positively correlated, and have a larger variance than the fluxes before subtraction. This correlation and extra variance both vanish for an infinitely deep reference image, but since we will not have an infinitely deep reference, the precision of light curve amplitude measurements is degraded with respect to this ideal case. We detail in Appendix B the computation of the effect, and will come back later to its practical implications.

Beyond the contribution to shot noise, differential photometry might also contribute to systematic uncertainties, especially in the context of ground-based image sets with sizable variations of image quality. Tests on real images from a ground-based SN survey (Astier et al. 2013) show that it is possible to obtain systematic residuals below 2 mmag, hence negligible compared with calibration uncertainties. The same tests show that the observed scatter of SN measurements follows the expected contributions from shot noise.

3.3. Supernova simulator

To simulate SNe Ia, we primarily made use of the SALT2 model (Guy et al. 2007, 2010). This model is a parametrised spectral sequence, empirically determined from photometric and spectroscopic data. We also made use of the brighter-slower and brighter-bluer relations determined from the SNLS3 SN sample (Guy et al. 2010), and the average absolute magnitude $M_B = -19.09 + 5 \log_{10}(H_0/70 \text{ km s}^{-1}/\text{Mpc})$ in the Landolt (i.e. Vega) system. Because of limitations of its training sample, SALT2 does not cover restframe wavelengths redder than 800 nm.

SALT2 parametrises events with 4 parameters: a date of maximum light (in B-band) t_0, a colour c, a decline rate parameter X_1 and an overall amplitude X_0. The latter is often expressed as m_B^*, the peak magnitude of the light curve in the redshifted B-band. Given these parameters, a redshift and a luminosity distance, we can evaluate fluxes of the SN in the observer filter at the required phase, and evaluate the uncertainty of the measurement, for the adopted instrumental setup and given observing conditions. Varying the cosmology only alters X_0 (or m_B^*), and in the simulations, we have assumed that the current uncertainties on the expansion history are now small enough to ignore the changes of measurement uncertainties when varying the cosmology.

SALT2 does not assume any relation between brightness and redshift. In the training process, the X_0 of events are nuisance parameters. This allows one to decouple distance estimation from light curve fitter training, and more importantly to train the light curve fitter using data at unknown distance. Thus, the SALT2 trainings (Guy et al. 2007, 2010) use a mixture of nearby events (including very nearby events where the redshift is a poor indicator of distance) and well-measured SNLS events. Since the statistical uncertainty of the model eventually contributes to the cosmology uncertainty, one has to minimise the former. In what follows, we will emulate the LC fitter training in order to incorporate the uncertainties that arise from this process into the cosmology uncertainties. We note that the light curve fitter training suffers from both statistical uncertainties (from the size and quality of the training sample) and from systematic uncertainties (typically the photometric calibration).

SALT2 is not a perfect description of SNe Ia, and there remain some variability of light curves around the best fit to data, beyond measurement uncertainties. This scatter depends on the adopted supernova model and was determined for SALT2 in

Guy et al. (2010). The residual scatter is described there as a coherent move around the average model of all light curve points of each band of each event, and it is found to depend on the rest-frame central wavelength of the band. This scatter is measured to about 0.025 mag rms in BVR-bands and increases slowly towards red and very rapidly in the UV (Fig. 8 from Guy et al. 2010). This scatter (coined "colour smearing" in Kessler et al. 2009) is accounted for in the simulation, and causes the difference between the two sets of points in our Fig. 2. Kessler et al. (2013) considers other colour smearing models than the SALT2 one and finds that this does not have a dramatic effect on the recovered cosmology. We note that the sample size we are considering in this paper will allow us to considerably narrow down the range of acceptable colour smearing models.

For the rate of SNe, we use the volumetric rate from Ripoche (2008)

$$R(z) = 1.53 \times 10^{-4} \left[(1+z)/1.5\right]^{2.14} h_{70}^3 \text{ Mpc}^{-3} \text{ yr}^{-1}, \quad (2)$$

where years should be understood in the rest frame. Since these measurements stop around $z = 1$, rates at higher redshifts were assumed to become independent of z. These rates compare well with the determination from Perrett et al. (2012). The rates proposed in Mannucci et al. (2007) (accounting for events "lost to extinction") yield a SN count (to $z = 1.5$) ~25% larger than our nominal assumption, with a similar redshift distribution. There are determinations of SN Ia rates at $z > 1$ from the Subaru deep field (Graur et al. 2011), and from the CLASH/Candels survey (Graur et al. 2014; Rodney et al. 2014), which are compatible with each other (see e.g. Fig. 1 of Rodney et al. 2014), and show that our assumption of rates flattening at $z = 1$ is likely conservative at the 20 to 30% level. We will discuss later (Sect. 5.1) other sources of uncertainty affecting the expected number of high-redshift events and will eventually derive how the cosmological precision depends on event statistics (Sect. 7.1). The redshift distribution of simulated events accounts for edge effects, i.e. we reject events at the beginning or the end of an observing season which do not have the full required restframe phase coverage.

The supernova simulation generates light curves in the user-required bands, at the user-required cadence, on a regular (redshift, colour, stretch) grid. For each band of each event, we evaluate the peak fluxes and the weight matrix of the four event parameters, by propagating the measurement uncertainty of all measurement points in this band, accounting for the effect of finite reference depth (Eq. (B.1)). These peak flux values and weight matrices are used by a global fit (Sect. 6 below) which will weight these events according to their redshift, colour and decline rate using measured distributions from Guy et al. (2010). The event weight also depends on the redshift-dependent SNe Ia rate (Eq. (2)), the edge-effect corrected survey duration, and the survey area. The colour smearing is accounted for during the global fit.

4. Supernova surveys

The SNLS survey has delivered its three-year sample, together with a cosmological analysis gathering the high quality SN sample and accounting for sytematic uncertainties (Guy et al. 2010; Conley et al. 2011; Sullivan et al. 2011). This compilation amounts to about 500 well-measured events, and will grow to about twice as much when SNLS and SDSS release their full samples, and gathering the nearby samples ($z < 0.1$) that appeared recently (e.g Stritzinger et al. 2011; Hicken et al. 2012; Silverman et al. 2012). Pan-STARSS1 has recently delivered a

Table 2. Depth of the visits simulated for the DESIRE survey.

	i	z	y	J	H
Depth (5σ)	26.05	25.64	25.51	25.83	26.08
Exp. time (s)	700	1000	1200	2100	2100

Notes. Depth (5σ for a point source) and exposure times at each visit for a 4-day cadence of the proposed DESIRE joint SN survey. The exposure times for LSST i and z bands assume nominal observing conditions. For *Euclid* NIR bands, the exposures times are the ones that would deliver the required depth in a single exposure, if such long exposures are technically possible. The S/N calculations are described in Appendix A.

first batch of 112 distances to SNe Ia at $0.1 \lesssim z \lesssim 0.6$ (Scolnic et al. 2014a; Rest et al. 2014), corresponding to 1.5 y of observations. The next significant increase in statistics is expected from the Dark Energy Survey (DES), which aims at delivering ~3000 new events in a 5-year survey extending to $z \sim 1.2$ (Bernstein et al. 2012), to which we compare our proposal in Sect. 8. To make significant improvements, a SN proposal for the next decade should target at least 10^4 well-measured events and should aim at significantly increasing the redshift lever arm.

4.1. High-z SN survey with Euclid: the DESIRE survey

As discussed in the introduction, measuring accurate distances to SNe at $z > 1$ requires to observe from space in the NIR. With its wide-field NIR capabilities, *Euclid* offers a unique opportunity to deliver a large sample in this redshift regime. In this section, we present the DESIRE survey (Dark Energy Supernova Infra-Red Experiment) which will be a dramatic improvement in the number of high quality SNe Ia light curves at redshifts up to 1.5.

Euclid observing time will be mostly devoted to a wide survey of 15 000 deg^2, with a single visit per pointing (Laureijs et al. 2011). Each single visit consists of 4 exposures for simultaneous visible imaging and NIR spectroscopy, and 4 NIR imaging exposures of 79, 81 and 48 s in y, J and H respectively. We refer to this set of observations as the "*Euclid* standard visit". The *Euclid* observing plan also makes provision for deep fields, which consist of repeated standard visits, in particular in order to assess the repeatability of measurements from actual repetition rather than from first principles. We attempted to assemble a SN survey from these repeated standard visits and failed to find a compelling standalone SN survey strategy. Our unsuccessful attempts are described in Appendix C.

Since we aim at measuring 3 bands per event, and require that these 3 bands map similar restframe spectral regions at all redshifts, we need to observe in more than 3 observer bands in order to cover a finite redshift interval. The obvious complement to *Euclid* consists of i- and z-bands observed from the ground. We identify at least three facilities capable of delivering these observations: LSST (8 m, Ivezic et al. 2008), the Dark Energy Camera (DECam) on the CTIO Blanco (4 m, Flaugher et al. 2010), and Hyper Suprime Cam (HSC) on the Subaru (8 m, Miyazaki et al. 2012). The most efficient of these three possibilities is LSST; HSC would require about 3 times more observing time than LSST while DECam would require about 10 times more. While these are all plausible options, we consider LSST to be the most natural partner and we chose it to illustrate the DESIRE survey in the remainder of this paper.

In Table 2, we display the depth per visit that delivers the required quality of light curves up to $z = 1.5$ (for an average SN). This table also lists observing times derived using our instrument
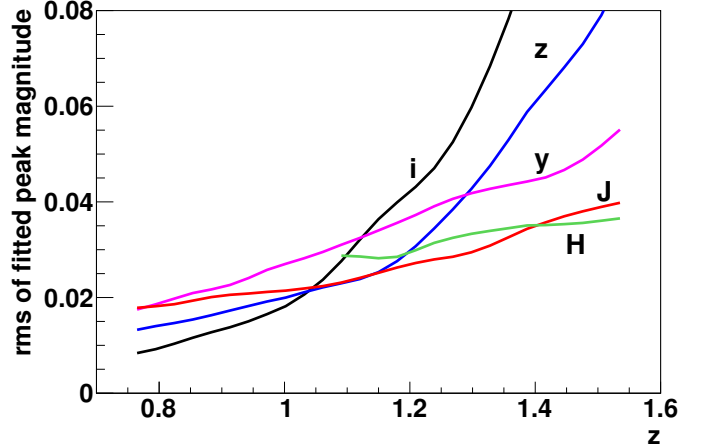

Fig. 5. Precision of light curve amplitudes as a function of redshift for the 5 bands of the DESIRE survey, assuming a 4-day cadence with the exposure times of Table 2. To fulfill the requirements in Sect. 2.3, i-band is used up to $z = 1$, z-band up to $z = 1.2$, and distances at $z = 1.5$ rely mostly on J- and H-band. For y, J and H bands, these calculations assume a reference image gathering 60 epochs in *Euclid*.

simulator. For i and z band, we used the sensitivities used for LSST simulations from Ivezic et al. (2008), however without accounting for the IQ degradation with air mass: somewhat longer exposure times might be needed in order to reach the required sensitivities. As for the *Euclid* observations, a slower cadence could be accommodated provided the depth per visit is increased accordingly. The derived precision of single-band light curve amplitudes of average SNe Ia are displayed in Fig. 5. Examples of simulated light curves are shown in Fig. 6.

We have assumed that *Euclid* could devote 6 months of its programme to monitor this dedicated deep field, possibly within an extended mission. The NIR exposure times in Table 2 add up to 5400 s per visit and pointing. Monitoring 20 deg^2 (40 pointings) at a four-day cadence uses 62.5% of the wall clock time for integrating on the sky. The rest is available for overheads such as readout, slewing, etc. Since building SN light curves require images without the SN, the programme is split over two seasons with identical pointings, so that each season, which consists of 45 visits, provides a deep SN-free image for the other season. Thus, our baseline programme consists of two six-month seasons, where the SN survey is allocated half of the clock time. In practice, this means that the same 10 deg^2 field will be observed twice, in two 6-month seasons during which the field should be visible from the ground. Within this scheme, the reference images (i.e. images without the SN) gather on average 1.5 observing season (i.e. 67 epochs for a 4-day cadence). We accounted for the finite reference depth effect of *Euclid* images assuming a 60-epoch reference (i.e. 1.3 season), following the algebra provided in Appendix B. Regarding reference depth, the situation for ground-based surveys is different since those are planning 5 (for the DES SN survey, see Bernstein et al. 2012) to 10 (for LSST, see Ivezic et al. 2008) observing seasons on the same field. The effect then amounts to a less than 10% degradation of amplitude measurements due to shot noise, which is sub-dominant in most of the redshift range, and we neglected the effect.

Regarding light curves in *Euclid* bands, we varied the reference depth in order to assess the acceptable variations of this parameter, and we display the impact of different reference depths in Fig. 7. Beyond 45 epochs (i.e. one season), the actual number
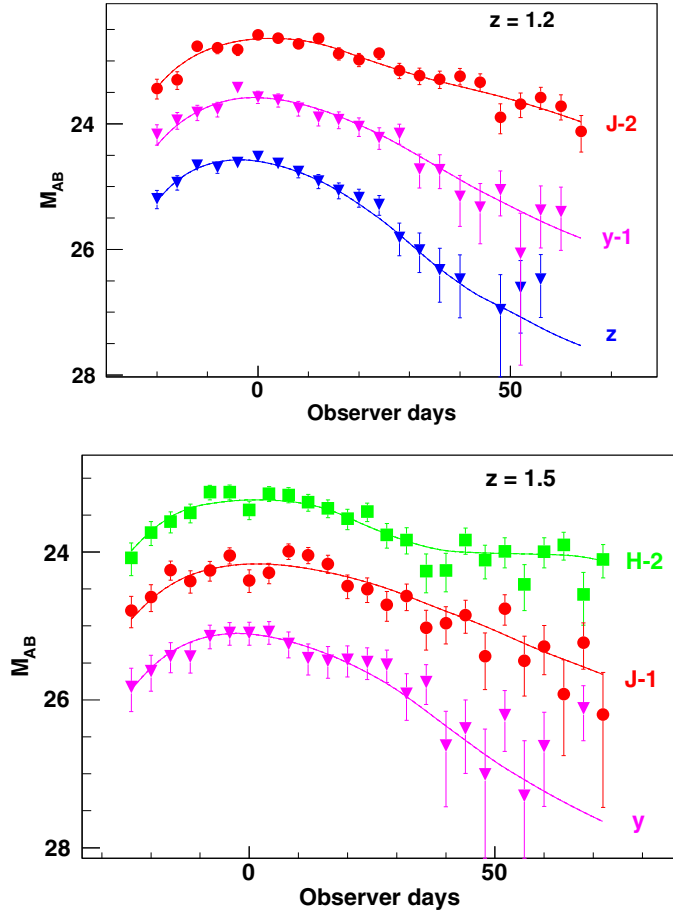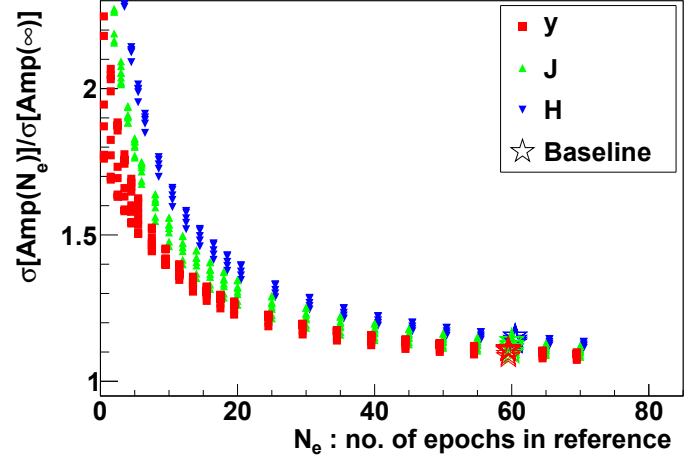
Fig. 7. Precision of light curve amplitude measurement, in units of the measurement quality for an infinitely deep reference, as a function of the number of epochs N_e used in the reference image. For each band, the spread at a given reference depth is due to redshift ($0.75 < z < 1.55$), and the effect increases with redshift. If all events were measured using 45 reference epochs (i.e. one season), the measurement precision would degrade by less than 10% relative to the chosen baseline, i.e. 60.

Table 3. Simulated depths per visit of the LSST Deep Drilling Fields.

	g	r	i	z	$y4$
depth (5σ)	26.47	26.35	25.96	25.50	24.51
Exp. time (s)	300	600	600	780	600

Notes. The exposure times refer to dark and otherwise average observing conditions. The $y4$ filter is the widest considered option for the LSST y-band.

Fig. 6. Simulated light curves of an average SN at $z = 1.2$ (*top*) and $z = 1.5$ (*bottom*).

does not make a large difference with our baseline. On the contrary, scenarios with a reference shallower than 15 to 20 epochs seriously degrade the measurement quality.

It is mandatory that the chosen field is observable by both *Euclid* and a ground-based observatory. The former imposes a field close to the ecliptic poles. The southern ecliptic pole suffers from Milky Way extinction and a high stellar density, but there are acceptable locations within 10° from the pole, observable for 6 months or more from the LSST site. The amount of observing time for LSST is modest, and could even be included as one of its "deep-drilling fields", which are already part of its observing plan. DECam on the CTIO Blanco could likely deliver the required sky coverage and depth in less than a night every 4th night. The northern ecliptic pole is observable by the Subaru telescope.

4.2. Other SN surveys by the time Euclid flies

By the time *Euclid* flies, we expect that the Dark Energy Survey (DES) will have produced a few thousand supernovae extending to $z \sim 1$ (Bernstein et al. 2012). LSST is not constructed yet, but it is expected to be a massive producer of SN light curves in the visible. LSST can tackle two redshifts regimes. First is the $0.2 \lesssim z \lesssim 1$ regime already covered by ESSENCE (Wood-Vasey et al. 2007), SNLS (Sullivan et al. 2011), and Pan-STARSS (Scolnic et al. 2014a; Rest et al. 2014), and by DES in the near future. Second is the "nearby" redshift regime, where LSST's large étendue and fast readout allow it to rapidly cover

large areas of sky. We now sketch a plausible contribution of LSST to the Hubble diagram of SNe Ia in these two redshift regimes.

4.2.1. LSST deep-drilling fields

The LSST deep-drilling fields (DDF) observations cover several scientific objectives, including distances to SNe. The current baseline for the observations consists of an approximately 4 day cadence with exposure times provided in Table 3. The corresponding fitted amplitude precisions are displayed in Fig. 8. The limiting redshift for a three-band measurement above 380 nm (restframe) is $z \simeq 0.95$, where the quality of r-band is more than adequate for identification. We note that the precisions displayed in Fig. 8 leave a good margin for less-than-optimal observations: a moderate degradation of image quality or time sampling would not affect our conclusions.

The volume of LSST deep-drilling fields observations adequate for distances to SNe is not settled yet but the current goal consists of monitoring 4 fields for 10 seasons. We conservatively assumed the statistics corresponding to 4 fields (each of 10 deg²) monitored over five 6-months seasons. 5 fields over 4 seasons yield the same event statistics.

4.2.2. Low-redshift supernovae with LSST

Cosmological constraints from relative distances enormously benefit from a local measurement and essentially all cosmological constraints from the Hubble diagram of SNe Ia make use
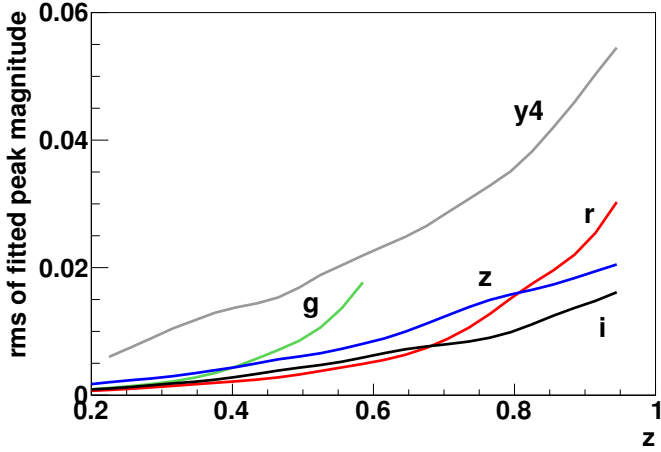
Fig. 8. Precision of light curve amplitudes as a function of redshift for the 5 bands of the LSST deep-drilling-fields survey, assuming a 4 day cadence with the depths from Table 3. At the anticipated depth, the contribution of the $y4$ band is marginal for distances to SNe. It however provides us with 3 bands within requirements at the highest redshift.

Table 4. Main parameters of the simulated surveys.

	z_{min}	z_{max}	Area (deg^2)	Duration (months)	Events
DESIRE	0.75	1.55	10	2×6	1740
LSST-DDF	0.15	0.95	50	4×6	8800
Low z	0.05	0.35	3000	6	8000

Notes. The duration of the DESIRE survey is two times 6 months, but the *Euclid* observations use only half of the clock time, and so add up to 6 months of clock time.

of a nearby SN sample. Since the relative calibration between surveys is currently a serious limitation (see e.g. Conley et al. 2011), we might wonder whether LSST itself might collect such a nearby sample. The LSST wide survey is built from two 15 s exposure visits (Ivezic et al. 2008), and covers 20 000 deg^2. The depth required to measure the shear field and photometric redshifts for galaxies is eventually obtained from several hundred exposures. If these exposures are evenly spread over 10 years, the time sampling is too coarse to measure distances to SNe Ia. We argue here that an uneven time sampling would allow us to monitor some fields with a 4 day cadence within the same overall time allocation (and hence final depth): one or more seasons observed at a ~4-day cadence using the regular LSST observing block (2×15 s) would deliver a depth per visit slightly higher than the SDSS-II SN survey (Kessler et al. 2009; Sako et al. 2014). Since LSST aims at monitoring 20 000 deg^2 for 10 years, we conservatively assumed that a proper cadence for SNe might be acquired over 3000 deg^2 for 6 months, which amounts to ~10 times the volume of the SDSS-II SN survey. We only consider events at $0.05 < z < 0.35$ where the quality is safely within requirements of Sect. 2.3. The lower redshift bound eliminates worries about peculiar velocities significantly affecting redshifts. The upper redshift bound derives from the cadence we have assumed and the depth of LSST visits. We note that this kind of observing strategy is not adopted yet within LSST, although it is actively studied. It might be implemented because it allows for additional science that cannot be done with evenly distributed sampling, and with no additional observing time.

The imposed quality requirements imply that all surveys are able to detect many events beyond their assigned high-redshift cutoff. This allows us to work in the redshift-limited regime in order to capture a similar fraction of the SN population at all redshifts. To summarise, we provide the main parameters for the three surveys in Table 4.

5. Redshifts and SN classification

5.1. Redshifts

With the statistics we are considering, we cannot expect to classify spectroscopically all events entering the Hubble diagram, as most of the SN surveys have done up to now. Spectroscopy

remains, however, the only way to acquire an accurate redshift, and we will assume in what follows that host galaxy spectroscopic redshifts are acquired at some point, possibly after the fact, using multi-object spectroscopy. The 4MOST and DESI projects on 4 m telescopes would both be well suited to obtaining spectroscopic redshifts of the majority of the host galaxies, as demonstrated by the sucessful use of the AAOmega instrument on AAT to observe host galaxies from SNLS (Lidman et al. 2013). Host galaxies remaining with unmeasured redshifts after such a campaign would be followed up with optical and infrared spectroscopy on 8 m or Extremely Large Telescopes.

In order to evaluate the required exposure times to acquire host redshift with a multi-object spectrograph, and the efficiency at obtaining host redshifts in SN surveys, we have studied how spectroscopic redshifts were assigned to a subsample of the SNLS events. We have selected SNLS spectra to $0.5 < z < 1$, which can be "translated" to $0.75 < z < 1.55$ by multiplying luminosity distances by 1.65, in order to emulate collection of host redshifts in the DESIRE survey. We have examined 40 slit spectra of "live" SNe collected using FORS2 on the VLT, and the origin of redshift determination splits this "training" sample into three event classes:

- 20 events happened in emission line galaxies (ELGs) where the redshift was obtained from the [O II] doublet (3726 and 3729 Å, unresolved with FORS2). We have then measured the [O II] line intensity.
- 11 events happened in passive hosts and the redshift was obtained from the Ca H & K absorption lines (3933 and 3968 Å). In these cases, we collected the host magnitudes from imaging data.
- 9 events did not have enough galaxy flux in the slit and were assigned a redshift using supernova features.

We note that both the [O II] doublet and the Ca H&K lines remain within the wavelength reach of (deep-depleted) silicon sensors at $z = 1.55$. In order to derive exposure times at higher redshifts than our SNLS subsample, we rely on the BigBoss (now called DESI) proposal (Schlegel et al. 2009). Namely, this proposal evaluates that with a 1000-s exposure time, it is possible to detect each member of the [O II] doublet at a S/N of 8 if the [O II] brightness is 0.9×10^{-16} erg/s, at a fairly extreme redshift of 1.75. Drawing from the SDSS experience, the same proposal relates passive supernova magnitudes and the exposure time required to get a redshift. We have "translated" the [O II] line brightnesses and host magnitudes of our test sample to higher redshifts by increasing the luminosity distance by 1.65, and using the BigBoss figures, we have evaluated that DESIRE emission line host galaxies would require up to 300 ks to deliver $S/N = 8$ per [O II] doublet member, and passive hosts would require up to 100 ks to deliver a redshift. Most of the hosts would require significantly less. These derived exposure times compare

well with the extrapolation of the typical ~3600 s on FORS2 of the SNLS spectra: this exposure time translates to ~100 ks for DESIRE host spectroscopy on DESI when accounting for the mirror size ratio (~2^2 for the diameter) and the fainter targets (~3^2). We find that the S/N requirement of the DESI proposal for [O II] emitters is higher than the ones we obtained for the faintest members of our training sample.

These exposure times might look large, but one should note that in Lidman et al. (2013), exposure times of 90 ks are reported. The redshift reach of the Lidman et al. (2013) pioneering programme does not extend significantly at $z > 1$, because it targeted hosts of SN candidates detected in the SNLS imaging data (Bazin et al. 2011), limited in redshift by the poor red sensitivity of the Megacam sensors (see e.g. Boulade et al. 2003). One might also note that the ultra deep VIMOS survey (50 ks exposures on the VLT) obtained a success rate at obtaining redshifts (Le Fevre et al. 2014) similar to our anticipation. Regarding the [O II] line brightness of SN hosts, three features indicate that our estimation is conservative; first, the SNLS spectroscopic campaign aimed at identifying live supernovae and the slit position was firstly aimed at maximising the SN flux, with less consideration for the host. Our training [O II] luminosities are then likely to be underestimated, as compared to fibre-fed spectroscopy targeting the host galaxy; second, the average [O II] brightness of ELGs tend to increase with z, and SN hosts likely follow this trend; third, as already mentioned, we are able to measure host redshifts at S/N lower than 8 per [O II] doublet member. So, we estimate that typically 75% of DESIRE host redshifts could be secured by means of multi-fibre spectroscopy in the visible. Fainter hosts could be targeted by more powerful instruments, and spectra of a subsample of the supernovae themselves (Sect. 5.2) almost unavoidably deliver redshifts.

One might consider the possibility of relying on photometric redshifts of supernovae. These are now known to be significantly more accurate than photometric redshifts of host galaxies (Palanque-Delabrouille et al. 2010; Kessler et al. 2010), thanks to the homogeneity of the events. SN photometric redshifts however introduce correlated uncertainties between distance and redshift which would require a careful study. SN photometric redshifts also degrade the performance of photometric identification and classification.

5.2. SN spectra

Spectra have been used to obtain detailed information on supernovae, mostly to empirically compare high- and low-redshift spectra (e.g. Maguire et al. 2012, and references therein). We can consider extending these comparisons to higher redshifts, relying on future facilities: both ground-based extremely large telescopes and the JWST will allow one to efficiently acquire NIR good-quality spectra of SNe Ia at $z \sim 1.5$ (Hook 2013). Using the available Exposure Time Calculators, we have evaluated exposure times of 900 s for the E-ELT, and 1500 s for prism spectroscopy using NIRSPEC on JWST to acquire a spectrum of an average SN Ia at $z = 1.55$, with a quality sufficient to compare spectral features with lower redshifts. We anticipate similar integration times with the 23 m Giant Magellan Telescope and the (30 m) Thirty Meter Telescope. These integration times are significantly lower than the typical 2 h required to identify a $z \sim 1$ SN Ia event using an 8 m class (ground-based) telescope.

In current surveys, SN spectra are primarily used to identify the events (see e.g. Howell et al. 2005; Zheng et al. 2008). Although we cannot hope to reproduce this strategy, obtaining SN spectra of a subsample will help characterise the transient

population and in particular the interlopers of the Hubble diagram. Given the exposure times above, assuming 40 h per semester awarded on both an ELT and JWST, and typically 30 mn per target including overheads, we could collect typically 300 live SN spectra. For the brightest targets, large programmes on existing 8−10 m telescopes could deliver ~200 spectra if 400 h could be gathered in total. So, collecting several hundred spectra of DESIRE events is a plausible goal.

5.3. SN classification

Most core-collapse supernovae are fainter than SNe Ia, and exhibit a larger luminosity dispersion. In Sect. 3.5 of A11, following arguments developed in Conley et al. (2011), it is shown that iteratively clipping to ±3σ the contaminated Hubble diagram yields acceptable biases to the distance redshift-relation, under various contamination hypotheses. This crude approach works because the contamination contribution to the Hubble diagram does not evolve rapidly with redshift. This crude typing conservatively assumes that light curve shapes and colours do not provide type information. Although all recent SN analyses indeed clip their Hubble diagram, we regard this purification through clipping as a backup plan, and we would prefer a selection based on colours and light curve shapes as proposed in e.g. Bazin et al. (2011); Sako et al. (2011); Campbell et al. (2013). The high photometric quality requirements we are imposing are an obvious help in this respect. Any method used to purify the Hubble diagram sample will be cross-checked using spectra of a subsample of active SNe, see Sect. 9.2.

6. Forecast method

In order to derive cosmological constraints, we follow the methods developed for A11, with the aim of accounting as precisely as possible for systematic uncertainties, including the interplay between different uncertainty sources. We will discuss astrophysical issues associated with SNe Ia distances in Sect. 9, and discuss here uncertainties mostly associated with the measurements themselves. In our forecast, we account for photometric calibration uncertainties, statistical light curve model uncertainties (because the training sample is finite), and photometric calibration uncertainty of the training sample, residual scatter around the model, fit of the brighter-slower and brighter-bluer relations, and make some provision for irreducible distance errors. We account for systematic uncertainties using nuisance parameters, and build a Fisher matrix for all parameters (including SN event parameters) that we invert in order to extract the covariance of the cosmological parameters. This gives us cosmological uncertainties marginalised over all other parameters. The method is detailed in A11 and we list now the considered uncertainty sources (and their size when applicable):

- The measurement shot noise.
- Statistical uncertainties of the light curve model. We assumed that it is trained on the cosmological data set.
- Systematic uncertainties due to flux calibration, both on SN parameters and through the SN model training. Our baseline assumes that the conversion of measured counts to physical fluxes is uncertain at the 0.01 mag level rms, independently for each band in visible and NIR. This level is conservative for the visible range considering the accuracy reached in Betoule et al. (2013). The impact of varying the photometric calibration accuracy is discussed in Sect. 7.1.

- The intrinsic scatter of supernovae at fixed colour (called colour smearing). We assign (magnitude) rms fluctuations of broadband amplitudes of 0.025, following Fig. 8 of Guy et al. (2010). We note that a more optimistic value $\sigma_c = 0.01$ was assumed in Kim & Miquel (2006). Larger smearings are indeed observed in the UV, but we ignore bands with $\bar{\lambda} < 380$ nm (where $\bar{\lambda}$ is the central wavelength of the filter).
- We fit for both brighter-slower and brighter-bluer relations and marginalise over their coefficients.
- We assume an intrinsic distance scatter of 0.12 mag, where current estimates are around or below 0.10 (Guy et al. 2010). The average Hubble diagram residual is about 0.14 rms, where the difference to 0.12 is mainly due to colour smearing.
- We assume that there is an irreducible distance modulus error, affecting all events coherently, varying linearly with redshift,

$$\delta\mu = e_M \times z, \tag{3}$$

with a Gaussian prior $\sigma(e_M) = 0.01$. This distance modulus error accounts for possible evolution of SNe Ia with redshift, not accounted for by the distance estimator, which in turn biases the measured distance-redshift relation. In A11 (Sect. 5.2), a metallicity indicator relying on UV flux is proposed that allows one to control the distance indicator at the level of ~0.01. Our ansatz above (Eq. (3)) makes provision for $\delta\mu = 0.015$ over the whole redshift range.

These uncertainties describe current know-how, in a rather conservative way. It is thus likely that we might eventually do better. The code that implements the global fit successfully reproduces the SNLS3 uncertainties.

In order to propagate uncertainties, we introduce nuisance parameters in the fit (e.g. alteration to the photometric zero points) and eventually marginalise over those. In order to emulate the light curve fitter training and the impact of calibration uncertainties, event parameters are also fitted, together with offsets to the fiducial SN model. Appendix A of A11 compares the propagation of uncertainties and the introduction of nuisance parameters and concludes that both approaches are strictly equivalent. Our global fit thus considers 5 sets of parameters:

- The event parameters in their SALT2 flavour: t_0 is a reference date, X_0 is the overall brightness, X_1 indexes light curve shape, and c is a rest-frame colour.
- The photometric zero points, or more precisely offsets to their nominal values. We impose priors on these offsets which account for photometric calibration accuracy, from SN instrumental fluxes to physical fluxes.
- The global parameters $(\alpha, \beta, \mathcal{M})$ used to derive a distance from the SN parameters:

$$\mu = m_B^* + \alpha X_1 - \beta c - \mathcal{M}. \tag{4}$$

Following Eq. (3), we emulate an irreducible fully correlated distance error with

$$\mathcal{M} = \mathcal{M}_0 + e_M \times z, \tag{5}$$

where e_M is constrained with a Gaussian prior of rms 0.01. The actual parameters are hence $(\alpha, \beta, \mathcal{M}_0, e_M)$. The overall flux scale of the Hubble diagram is unknown and $\mathcal{M}_0$, which is marginalised over, accounts for it.

- The supernova model definition. We model both the peak brightness of the average SN as a function of wavelength, and how colour variations affect different wavelengths (see Sect. 4.3.3 of A11). For both quantities we model offsets to the fiducial SN model, using 10-parameter polynomials over the SN model restframe spectral range, which makes more than 2 parameters per regular broadband filter. These parameters account for the SN model training.
- The cosmological parameters.

SN cosmology usually proceeds in two steps: first extracting event parameters by fitting a model to light curves, and then fitting cosmology to distances derived from these event parameters. With calibration uncertainties at play, the first step results in fully correlated event parameters, but the correlations due to systematics are in fact a small-rank matrix, compared to the number of events we are considering here. Instead of this two-step procedure, we carry out both steps simultaneously summing all terms in a single χ^2, where the light curve fit term also incorporates the light curve fitter training. This method is equivalent to the two-step procedure but does not require propagating a large covariance or weight matrix between stages. The fit involves a large number of parameters (more than 50 000) and the Appendix B of A11 sketches the method used to compute the covariance matrix of a small subset of parameters, among which are the cosmological parameters.

7. Forecast results

In order to evaluate the cosmological constraints that the proposed surveys could deliver, we use the commonly used equation of state (EoS) effective parametrisation proposed in Chevallier & Polarski (2001): $w(z) = w_0 + w_a z/(1+z)$, and shown to describe a wide array of dark energy models in Linder (2003). We define the cosmology with two more parameters: Ω_M the reduced matter density, and Ω_X the reduced dark energy density, both evaluated today. Distances alone do not constrain efficiently these 4 parameters, and in practice, at least two external constraints have to be added. We have settled for one CMB prior, taken as a measurement of the shift parameter $R \equiv \Omega_M^{1/2} H_0 r(z_{\mathrm{CMB}})$, and flatness. For the geometrical CMB prior, we compared the R measurement to 0.32% (anticipated from *Planck*, see Mukherjee et al. 2008, Table 1), with the binned w matrix for CMB alone from Albrecht et al. (2009) projected on the (w_0, w_a) plane in a flat Universe, and found extremely similar results. Both approaches take care to ignore information on dark energy from the ISW effect in the CMB, because the latter concentrates on large angular scales and might be difficult to extract. We also wish to ignore the ISW effect in order to ensure a purely geometrical cosmological measurement that is insensitive to the growth of structures after decoupling. The method also ignores potential information from CMB lensing. We describe in Appendix E how to obtain SN-only constraints from our results.

We simulate distances in a fiducial flat ΛCDM Universe with $\Omega_M = 0.27$. We restrict the rest frame central wavelength of the bands entering the fit to [380−700] nm, which leaves 3 to 4 bands per event. Enlarging this restframe spectral range formally improves the statistical performance but breaks the requirement that similar rest frame ranges are used to derive distances at all redshifts.

The quality of EoS constraints are usually expressed, following Albrecht et al. (2006), from the area of the confidence contours in the (w_0, w_a) plane, and the normalisation we adopt reads $FoM = [Det(Cov(w_0, w_a))]^{-1/2}$. Still following
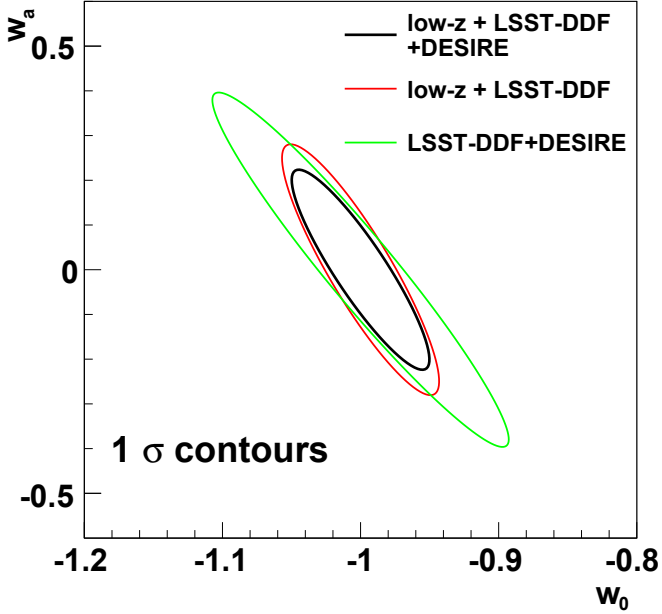
Fig. 9. Confidence contours (at the 1σ level) of the survey combinations listed in Table 5. The assumptions for systematics correspond to the last row of Table 6.

Table 5. Cosmological performance of the simulated surveys.

	$\sigma(w_a)$	z_p	$\sigma(w_p)$	FoM
low-z + LSST-DDF + DESIRE	0.22	0.25	0.022	203.2
low-z + LSST-DDF	0.28	0.22	0.026	137.1
LSST-DDF + DESIRE	0.40	0.35	0.031	81.4

Notes. The FoMs assume a 1D geometrical *Planck* prior and flatness. z_p is the redshift at which the equation of state uncertainty reaches its minimum $\sigma(w_p)$. The FoM is defined as $[\mathrm{Det}(Cov(w_0, w_a))]^{-1/2} = [\sigma(w_a)\sigma(w_p)]^{-1}$ and accounts for systematic uncertainties. The contributions of the main systematics are detailed in Table 6.

Albrecht et al. (2006), we define the pivot redshift z_p to be where the EoS uncertainty is minimal, and $w_p \equiv w(z_p)$. $\sigma(w_p)$ is also the uncertainty when fitting a constant EoS. $\sigma(w_p)$ can be regarded as the ability of the proposed strategy to challenge the cosmological constant paradigm. In Table 5, we report the following performance indicators: $\sigma(w_p)$, the uncertainty of the EoS evolution $\sigma(w_a)$, and the FoM. The FoM difference between the two first lines shows the *Euclid* contribution to the overall FoM: by delivering about 10% of the total event statistics (see Table 4), the high redshift *Euclid* part of the Hubble diagram increases the FoM by ~50%. The confidence contours corresponding to Table 5 rows are displayed in Fig. 9.

We present in Table 6 some combinations of uncertainties, and we find (as in Table 5 of A11) that the dominant reduction in the figure of merit arises from the combination of calibration uncertainties and SN model training. In A11, we also considered the impact of several hypotheses such as fitting the α and β parameters (Eq. (4)) separately in redshift slices, or assuming that there are several event species, each with its light curve model and $(\alpha, \beta, \mathcal{M}_0, e_M)$ set, and concluded that these extra parameters result in negligible degradation of the cosmological precision.

The event statistics of the DESIRE survey is primarily limited by the amount of time available on *Euclid*, and is hence
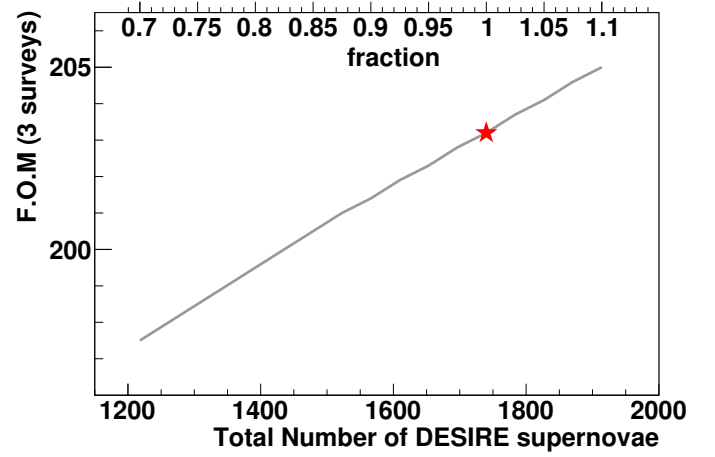
Fig. 10. FoM for the 3 surveys as a function of the SN statistics in DESIRE. The upper horizontal scale is the fraction of events actually entering into the Hubble diagram, with respect to our baseline assumptions. Event rate measurements at $z > 1$ (see Sect. 3.3) suggest higher statistics (by ~20%) than we assumed, and the efficiency at getting host redshifts could eliminate 25% of the events. In any case, we see that the cosmological performance does not depend critically on these numbers.

Table 6. Cosmological performance with various uncertainty sources.

Assumptions						
cal	evo	train	$\sigma(w_a)$	z_p	$\sigma(w_p)$	FoM
n	n	n	0.15	0.30	0.016	418
y	n	n	0.18	0.30	0.016	339
n	y	n	0.18	0.25	0.018	315
y	y	n	0.20	0.27	0.019	266
n	n	y	0.16	0.30	0.016	403
n	y	y	0.18	0.25	0.018	304
y	n	y	0.21	0.28	0.020	238
y	y	y	0.22	0.25	0.022	203

Notes. "cal" refers to calibration uncertainties ($\sigma_{ZP} = 0.01$). "evo" refers to evolution systematics (Eq. (3)). "train" refers to SN model training from the same sample.

not extensible. It is then important to assess the impact of lower statistics on the cosmological performance. We remind here that rates at $z > 1$ are uncertain (but we have adopted a conservative approach), and that we have evaluated that a massively parallel spectroscopic campaign to collect DESIRE host redshifts could reasonably target a ~75% completion rate (see Sect. 5.1). We show in Fig. 10 that the cosmological performance is not severely affected by a significant decrease of the DESIRE event statistics actually entering into the Hubble diagram.

7.1. Altering the baseline survey and systematic hypotheses

The photometric calibration uncertainty (i.e. the zero point uncertainty) and the evolution uncertainty (Eq. (5)) constitute the two main performance drivers with a fixed SN sample size. Fig. 11 shows the cosmological performance as a function of the size of these systematic uncertainties. Regarding the photometric calibration, we have varied only the NIR calibration accuracy (i.e. *Euclid*'s photometric calibration), since photometric calibration accuracy in the visible is already better than what we assumed (see Betoule et al. 2013). We note that the
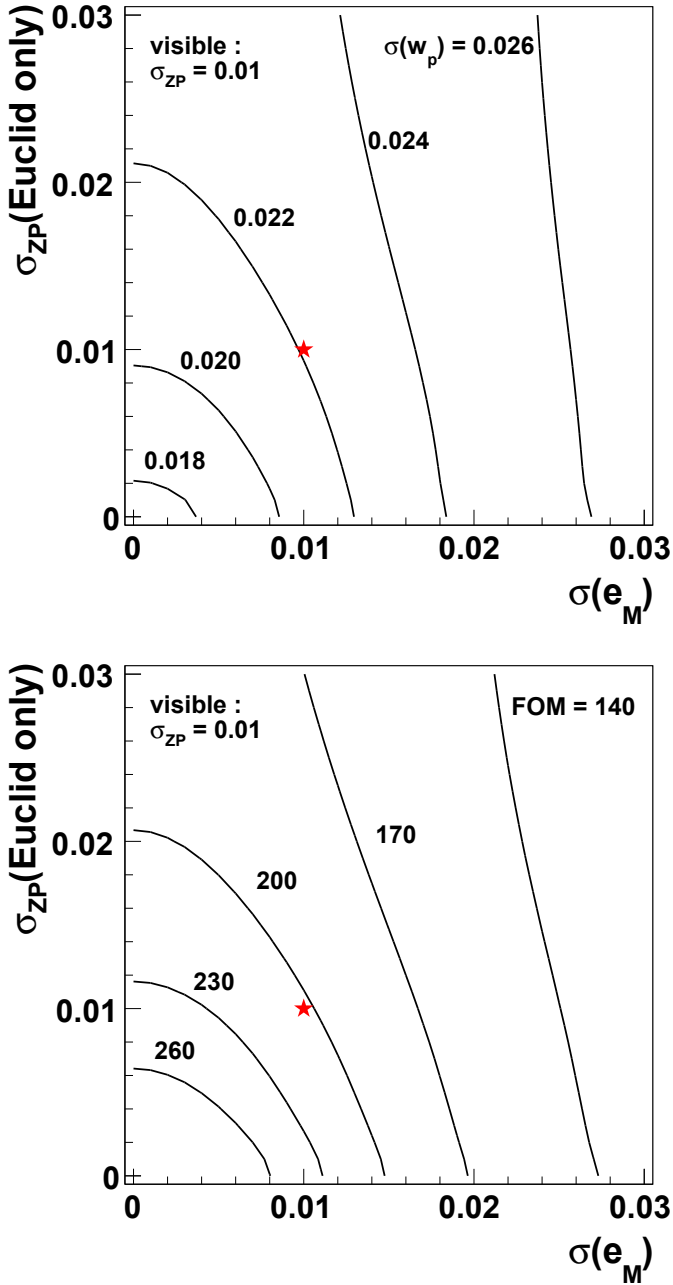
Table 7. Effect of altering some survey parameters.

Alteration	$\sigma(w_p)$	FoM
none	0.022	203
statistics (all surveys) $\times$ 1.25	0.021	231
statistics (all surveys) $\times$ 0.75	0.024	172
low-z $\times$ 1.25	0.022	218
low-z $\times$ 0.75	0.023	187
LSST-DDF $\times$ 1.25	0.022	212
LSST-DDF $\times$ 0.75	0.023	193
DESIRE $\times$ 1.25	0.022	208
DESIRE $\times$ 0.75	0.022	199
$\sigma_c = 0.015$	0.021	223
$\sigma_{int} = 0.10$	0.021	231
$\sigma_c = 0.04\ \sigma_{int} = 0$	0.022	204

Notes. σ_c refers to colour smearing (0.025 by default), σ_{int} refers to the Hubble diagram scatter (without any shot noise nor colour smearing), set to 0.12 in our baseline.

Fig. 11. Contour levels of $\sigma(w_p)$ (*top*) and the FoM (*bottom*) as a function of *Euclid* calibration accuracy σ_{ZP} (equal for all *Euclid* filters), and the distance evolution uncertainty $\sigma(e_M)$ (defined in Eq. (5)). The stars indicate our baseline (0.01, 0.01). One can note that significantly worse hypotheses do not dramatically degrade the capabilities of the proposed surveys.

performance is reasonably robust to significant changes in these two uncertainties.

We investigate how the performance varies with statistics in Table 7: the FoM varies roughly as the square root of the total number of events (rather than linearly without systematics nor external priors). By altering the overall statistics of each of our three surveys separately, we show that all three contribute similarly to the cosmological precision (as already indicated in Table 5). The DESIRE part shows the smallest relative change, mostly because it has the smallest number of events in a first place. We note that modest improvements of the SN modelling

quality (intrinsic scatter and colour smearing) significantly improve the overall performance.

Scolnic et al. (2014b) propose to describe the scatter around the brighter-bluer relation using $\sigma_c = 0.04$ and $\sigma_{int} = 0$, where we use by default respectively 0.025 and 0.12; transferring the scatter from brightness to colour also increases β from 3 to ~4. With this extreme setup, we find a FoM of 204, i.e. unchanged with respect to our baseline.

Rather than altering globally the statistics of the three proposed surveys, one may study how a small event sample at a given redshift improves the cosmological performance as a function of this redshift. With our setup, $z < 0.1$ is the most efficient redshift range, because we have less than 200 events at $0.05 < z < 0.1$ (see Fig. 12). Adding 200 supernovae at $z = 0.05$ improves the figure of merit by more than 30. However, incorporating a low-redshift sample into the analysis requires that it is measured in three bands in the B, V, R spectral region, that the photometry is precisely cross-calibrated with respect to other samples and that this nearby sample is essentially unbiased. The latter probably implies to collect it in the "rolling search" mode, which is a demanding requirement given the sky area that has to be patrolled for collecting 200 low-redshift SNe Ia. We have not incorporated such a sample in our forecast, but one could argue that existing facilities (e.g. PTF Law et al. 2009; Skymapper Keller et al. 2007) could deliver it soon.

8. Comparison with the DES and WFIRST SN survey proposals

Bernstein et al. (2012) present the forecasts for a SN survey to be conducted within the Dark Energy Survey (DES). This work anticipates about 3000 events with acceptable distances at $0.3 < z < 1.2$, complemented by a 300-event nearby sample and 500 events from the SDSS. The presented cosmological constraints incorporate a "DETF stage-II prior"[4], which accounts for more than just *Planck* constraints: on its own, this prior delivers a FoM of 58. The forecast does not account for uncertainties arising from SN model training. In order to compare our findings with this work, we compute our FoM in the same conditions: we temporarily adopt the same external prior, we ignore SN model training uncertainties, and we let the curvature float.

---

[4] We are grateful to R. Biswas for providing us with the weight matrix of this prior.
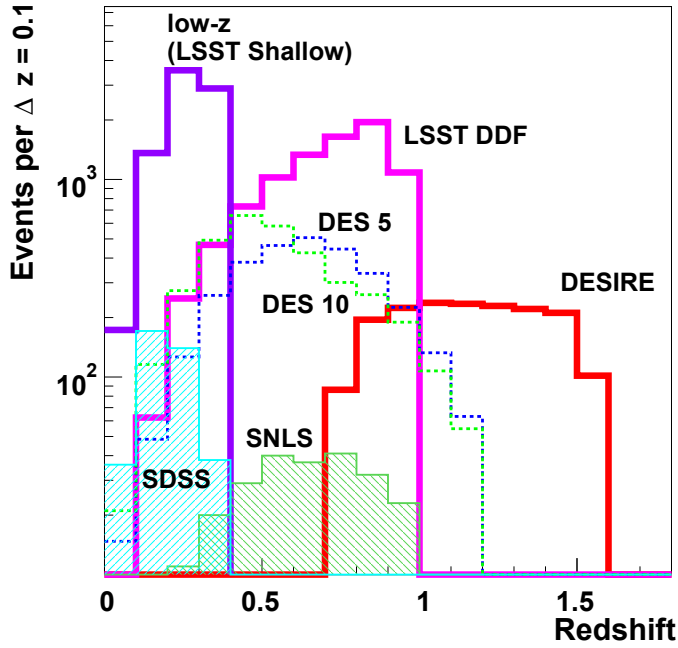
Fig. 12. Redshift distribution of events for various surveys. For the SDSS and SNLS, the distributions sketch the total sample of spectroscopically identified events eventually entering the Hubble diagram. "DES 5" and "DES 10" refer respectively to the "hybrid-5" and "hybrid-10" strategies studied in Bernstein et al. (2012), where the baseline is hybrid-10. "LSST-SHALLOW", "LSST-DDF" and "DESIRE" refer to the three prongs studied in this proposal.

Our assumptions about calibration uncertainties are already the same as those from Bernstein et al. (2012). We find a FoM of 468 for our 3 surveys, to be compared to 124 for the SN DES survey (Bernstein et al. 2012, Table 15). It is hence clear that our proposal constitutes a significant step forward after DES. We compare the redshift distributions of the DES planned observations with the current samples and our proposal in Fig. 12.

WFIRST is a NASA project of a NIR wide-field imaging and spectroscopy mission in space (Green et al. 2012, W12 hereafter). The mission is presented in two versions DRM1 and DRM2 with mirrors of 1.3 and 1.1 m diameter and durations of 5 and 3 years respectively. In both instances, the primary mirror is un-obstructed, which not only enhances its collecting power, but also allows for a more compact PSF than a conventional on-axis setup with the secondary mirror and its supporting structure in the beam. The baseline supernova survey (assuming DRM1, see W12 p. 34) makes use of 6 months of observing time spread over 1.8 y, and devotes more than two thirds of its observing time to low-resolution prism spectroscopy; the remainder is used for imaging in J, H and K bands every 5 days. This is a dual-cone survey, where the deep part targets $0.8 < z < 1.65$ and covers 1.8 deg^2, and the shallow part targets $z < 0.8$ over an area of 6.5 deg^2, to which one should add the contribution from the deep survey footprint. The integrations at each visit last 1500 s and 300 s in the two surveys. The forecast adds a nearby survey of 800 events (at typically $z < 0.1$). We thus have three redshift regimes which roughly gather (in increasing order) 800, 1400 and 700 events. The high-z part gathers about half of the statistics targeted by DESIRE, but extends to higher redshifts. The low-redshift part is very different from the one we have sketched: it is first at lower redshift and second should be measured in significantly redder bands (around 1 μm) than most current nearby samples (and our projected low-z part), in order to

Table 8. Our findings for the WFIRST SN survey performance, complemented by 800 nearby events.

Assumptions						
cal	evo	train	$\sigma(w_a)$	z_p	$\sigma(w_p)$	FoM
n	n	n	0.19	0.28	0.016	323
y	n	n	0.24	0.37	0.025	170
n	y	n	0.22	0.24	0.019	242
y	y	n	0.26	0.32	0.029	132
n	n	y	0.32	0.32	0.017	180
n	y	y	0.34	0.30	0.021	137
y	n	y	1.04	0.33	0.032	30
y	y	y	1.05	0.33	0.035	28

Notes. "cal" refers to calibration uncertainties ($\sigma_{ZP} = 0.01$). "evo" refers to evolution systematics (Eq. (3)). "train" refers to SN model training from the same sample. The same quantities for our proposal are shown in Table 6.

match the restframe bands of higher redshift events considered in the project. The intermediate part is also very different from our LSST-DDF sketch (or any ground-based $z < 1$ SN survey in the visible) because it measures in the NIR. It is not obvious that the project would significantly benefit from considering intermediate-redshift events measured in the visible from the ground, and the forecast concentrates on an essentially space-based programme.

The anticipated sensitivity of the instrument outperforms *Euclid* by more than 0.7 mag: a 1500 s integration with WFIRST reaches beyond $H = 26.7$ (5σ point source)[5] while *Euclid* remains below $H = 26$ (despite its wider H filter). The chosen strategy makes a very efficient use of this exquisite sensitivity by acquiring low-resolution spectra of all space-based events, which is not a plausible option for *Euclid*. The quality requirement for light curves is slightly stricter than ours: $S/N > 15$ at maximum light with a 5 day-cadence, while ours translates to $S/N > 12$ at maximum for the same cadence. The WFIRST survey design breaks our requirement regarding similar restframe wavelengths at all redshifts, because the span of the measurements in (J, H, K) (about a factor of 2 in wavelength) is narrower than the redshift range $0.1 < z < 1.65$ (i.e. $1 + z$ varies by about 2.4). Relative distances hence heavily rely on the SN model and are affected by calibration uncertainties of the training sample. In W12, systematic uncertainties of distances to SNe are modelled as independent in $\Delta z = 0.1$ bins with a value that matches the statistical accuracy from ∼50 events in the same bin at low redshift and ∼25 events at high redshift. With these assumptions and *Planck* priors, W12 find a FoM of about 150, which reaches 240 when systematic uncertainties are halved. The $z > 1.5$ part contributes less than 20 to the FoM (Fig. 18 of W12).

In order to compare the SN survey proposed in W12 to the present proposal, we apply our simulator to the WFIRST SN survey, in particular with our baseline systematic uncertainties. We have thus performed an approximate simulation of the 3-prong survey proposed in W12, and we note that we are in a regime where intrinsic fluctuations dominate over shot noise, and hence the details of the instrument sensitivity are not crucial. With our assumptions about rates, we find similar overall statistics to W12, larger for the high-z part by about 200 events, and lower for the mid-z part by the same amount. We do not regard this difference as important. Table 8 displays

---

[5] We computed the anticipated depth of a 1500 s SN visit from the reported depth $H = 29.6$ of the final stack of ∼130 epochs (W12, p. 10).

the cosmological performance we extract from our simulator, which is again strongly driven by assumptions about systematics at play. When considering uncertainties induced by photometric calibration and evolution, we find a FoM of ~130, very close to the value of ~150 found in W12, although we have assumed that uncertainties are correlated across redshifts. Because the rest-frame wavelengths are changing with redshift, the SN model cannot be extracted from the same sample, as indicated by the dramatic performance drop in the last rows of Table 8. For the proposed SN survey of W12, the observed SN fluxes as a function of redshift can be described by different associations of an SN model (i.e. flux as a function of wavelength) and a distance-redshift relation, and extracting both from the data yields large cosmological uncertainties. These large uncertainties motivate our strategy of extracting distances from the same rest-frame region at all redshifts. The projections in W12 assume, in contrast to ours, that the SN model has been developed elsewhere, and that the assumed systematic uncertainties make provision for all SN model uncertainties. For our proposal, we get a FoM = 266 if we ignore SN model uncertainties (see Table 6).

Recently, a new WFIRST concept has been proposed, relying on an existing 2.4m space-quality on-axis primary mirror. A scientific programme and an instrument suite taking advantage of this powerful telescope have been proposed (Spergel et al. 2013). The supernova programme still uses 6 months of observing time but follows a different route: SNe are discovered using the wide-field imager and their distance are estimated from a series of photometric $R \sim 100$ spectra ($0.6 < \lambda < 2 \ \mu$m) obtained using an Integral Field Unit. The SN programme acquire ~7 spectra of the SN at a 5-day cadence, and the equivalent of 4 epochs for the reference. The SN spectra deliver a S/N for synthetic broad-band photometry of about 15 per filter at each visit, except for one spectrum at maximum light that reaches $S/N \simeq 50$. Events are selected for spectro-photometric follow-up so that the redshift distribution is flat at $0.6 < z < 1.7$ with 136 events per $\Delta z = 0.1$, and more populated at lower redshifts. The forecast anticipates similar contributions of systematics and statistics, using the optimistic hypothesis for systematics from W12: the IFU instrument is assumed to be easier to calibrate than an imager, and using spectroscopy allows one to get rid of cross-redshift K-corrections. The forecast does not provide a figure of merit. It seems a priori very difficult to complement the proposed analysis using samples measured in the visible from the ground through imaging (as in our sketch), both because of the different measurement technique but also because of the different restframe wavelength coverage.

Both SN proposals for WFIRST aim at covering a redshift range wider than the spectral coverage of the instrument, and hence have to measure supernovae at different redshifts in different restframe spectral ranges. This makes both of them vulnerable to inaccuracies of the SN model used to relate these different restframe spectral regions. To get around this limitation, one either has to show that the incured uncertainties are negligible (our Table 8 indicates that it is not the case), or narrow the redshift range of the space project to match the wavelength coverage of the instrument. In this second hypothesis, all considered NIR space missions will have to complement their high-redshift samples with lower redshift events presumably from wide-field ground-based facilities.

Regarding the 2.4 m supernova survey project, it still has to be demonstrated that measuring flux ratios from an IFU can reach the required accuracy (typically a few 10^{-3}). On the other hand, one cannot question that a 2.4 m wide-field space mission has a farther reach than *Euclid* for distances to SNe, should

it eventually rely on the "traditional" and established imaging methods. The time line of this project remains uncertain.

9. Astrophysical issues

9.1. Host galaxy stellar mass

It has been shown that even after applying the brighter-slower and brighter-bluer relations, residuals of the Hubble diagram are correlated with host galaxy stellar mass (Kelly et al. 2010; Sullivan et al. 2010; Lampeitl et al. 2010). Obviously, the host galaxy stellar mass is a proxy for some physical source of the effect yet to be uncovered (see e.g. Gupta et al. 2011; Childress et al. 2013), possibly metallicity (D'Andrea et al. 2011; Hayden et al. 2013; Pan et al. 2013). In the first analyses considering this effect, ignoring it caused a sizable bias on w (e.g. about 0.08, Sullivan et al. 2011), mostly because low-redshift searches favour massive hosts, while rolling searches discover events regardless of the host properties. The "JLA" SN sample (Betoule et al. 2014) is composed at more than 80% by the SDSS and SNLS rolling searches, and when fitted together with *Planck*, ignoring the host mass dependent brightness shifts w by less than 0.01. This does not conflict with the 5σ detection of the host mass dependent brightness on this sample, but rather indicates that its host mass distribution evolves slowly with redshift. In the PS1 SN analysis (Scolnic et al. 2014a), the host-mass effect turns out to be barely detected.

The required host stellar mass precision is modest because the correction varies slowly with stellar mass (e.g. Fig. 3 of Sullivan et al. 2010). This host stellar mass is estimated using galaxy population synthesis models fitted to broad-band photometric measurements of host galaxies. As in past SN surveys, the surveys we are discussing in this paper offer the opportunity to gather this photometric data in typically 5 bands. Although it is likely that our understanding of the phenomenon will have improved by the time *Euclid* flies, the data required to account for the effect by current methods is indeed a by-product of the SN surveys, as experienced by current projects. The photometric depth obtained by stacking all DESIRE images (Sect. 10.2) seems sufficient for this purpose, considering that, as done currently, one can just assign a low stellar mass to apparently hostless SN events.

As discussed above and in A11, if the understanding of the effect requires separate models for SN subclasses, and/or separate α, β, and $\mathcal{M}$ for different stellar mass hosts, or some other quantity, as suggested in Hayden et al. (2013), the degradation of cosmological performance is negligible.

If obtaining host redshifts significantly selects among the event population (in particular in the DESIRE part), the analysis should take care at restoring similar host populations at all redshifts, typically in order to ensure that applying or not the chosen host correction does not have a serious effect on cosmological conclusions. This might in turn reduce the statistics of nearby and mid-redshift samples. For these samples, one should regard the event statistics we have considered as what is actually used for cosmology. We note that for both of these samples, our hypotheses are well below what the LSST instrument can plausibly deliver within its planned programme.

9.2. Spectroscopy of "live" supernovae and metallicity diagnostics

Almost all SN cosmology works so far have acquired a live spectrum of their events, but this is impractical for the sample size we

are considering here. We however still envisage collecting a sizable sample of SN+host spectra. This is known to be feasible at $z < 1$ (e.g. Zheng et al. 2008; Balland et al. 2009; Blondin et al. 2012). In the next decade, we can seriously consider extending the spectroscopic comparisons of SNe across redshifts and host types to higher redshifts than currently available: both the JWST and ground-based extremely large telescopes (Hook 2013) will provide relatively easy access to mid-resolution spectroscopy of faint targets ($m \sim 26$) in the NIR, not practical with current instruments. These facilities will allow us not only to extend the spectroscopic comparisons of SNe Ia to $z = 1.5$ and above, but also to characterise the contamination of the Hubble diagram across redshifts.

Among spectroscopic diagnostics of the chemical composition of the ejecta, assessing the details of the UV flux around 300 nm restframe is particularly useful to estimate the metallicity of the progenitor (Lentz et al. 2000; Foley & Kirshner 2013). UV spectroscopic measurements already exist at low redshift (Maguire et al. 2012), and at $z \simeq 0.6$ (e.g. Walker et al. 2012, and references therein). Extending the redshift range of such measurements should become possible. In A11 (Sect. 5.2) we proposed photometric measurements of SN metallicity through the broadband flux at $250 \lesssim \lambda \lesssim 320$ nm restframe. Such measurements allow one to control offsets of the distance modulus at the 0.01 level. In the surveys we are sketching, the data for such measurements is available at $z \simeq 0.7$ (g band) and again at $z \simeq 1.6$ (i band).

9.3. Colour relations and dust extinction

Although the fact that brightness and colours of supernovae are related is not debated, the physical source of this relation is still unclear. There are clear signatures of dust extinction in spectra of highly reddened events (e.g. Blondin et al. 2009 and Wang et al. 2009 and references therein), and some indications that part of the brighter-bluer relation could be intrinsic to supernovae (e.g. Foley & Kasen 2011). An intriguing observation is that the colour distributions seem similar across environments (Sullivan et al. 2010; Lampeitl et al. 2010), although one would expect less extinction in passive galaxies than in active ones. Smith et al. (2012) even provide some indication that supernovae in passive hosts are slightly redder than in star-forming hosts. It is thus likely that the observed brighter-bluer relation is a mixture of dust extinction and intrinsic SN variability. Most of the supernova cosmology analyses eliminate heavily reddened events, likely to be extincted by dust, because they are rare and faint, and could be atypical.

Since the brighter-bluer relation is linear in colour vs magnitude space, and different colours are related by linear relations (e.g. Leibundgut 1988; Conley et al. 2008) it is natural to adopt the formalism of extinction. In our analysis, we have adopted an agnostic approach, namely deriving the "extinction law" from data, without assuming that it belongs to the classical forms determined for dust in the Milky Way (Cardelli et al. 1989). In our approach, this law is separated in two parts: a polynomial function of wavelength, and the β parameter of Eq. (1). A determination of this law from spectroscopic SN data has shown that it is a smooth function of wavelength (Chotard et al. 2011), and we use a polynomial function with 10 coefficients to model it. As mentioned earlier, if the extinction law and/or the β parameter have to be determined separately for different event classes, the impact on the cosmological precision is either very small (A11) or even null in some cases (A11 Appendix C).

The case for a β parameter evolving with redshift is unclear (see e.g. the discussions in Kessler et al. 2009 and Conley et al. 2011). As in A11, we follow an agnostic route and evaluate the extra cost of fitting different β values in redshift bins: we find that fitting separate α and β parameters in $\Delta z = 0.1$ bins decreases the FoM by less than 1.

10. Other science with DESIRE

While the primary motivation for the DESIRE survey is precision cosmology with distant SNe Ia, the resulting images will enable a wealth of other science, both using the time series of images and using the final deep stacked images, from the bands aimed at measuring distances, but also from the sharp *Euclid* visible images which can be acquired simultaneously. It is beyond the scope of the present paper to explore in detail all the possible scientific legacy of DESIRE, but we will just mention a few examples.

10.1. Transient astrophysics

The large statistics of distant SNe Ia can be used to measure their rate evolution as a function of redshift. When compared to the cosmic star formation history (SFH), the rate evolution with redshift sets strong constraints on the Delay Time Distribution (DTD) of SNe Ia, and therefore provides information on their progenitors (e.g. Perrett et al. 2012; Maoz & Mannucci 2012; Maoz et al. 2014; Graur & Maoz 2013). This analysis will benefit from the comparison with the large transient statistics now available for the local Universe that is the harvest of a number of very successful SN searches, e.g. the Palomar Transient Factory (Rau et al. 2009) or the Catalina Real-Time Transient Survey (Drake et al. 2012).

Additional constraints on the progenitors scenario (Maoz et al. 2014) can be obtained by comparing the SNe Ia rates with the properties of the parent galaxies as obtained from broadband photometry (e.g. Mannucci et al. 2005, 2006; Sullivan et al. 2006; Li et al. 2011) or spectroscopy (Maoz et al. 2012). Besides the astrophysical interest, this analysis is important for the cosmological use of SNe Ia because it can help to control the systematics related to a possible evolution of these standard candles.

As well as SNe Ia, the DESIRE survey will discover >1000 core-collapse SNe that can also be used as cosmological distance indicators. In particular, Hamuy & Pinto (2002) found a tight correlation between the expansion velocity and plateau magnitude for II-Plateau SNe (IIP), which has since been extended to cosmologically useful redshifts (Nugent et al. 2006). Although fainter than SNe Ia, their progenitors are well understood and there is excellent potential for IIP to be used as complementary probes of the cosmological parameters in the NIR (Maguire et al. 2010).

In addition, the statistics of core collapse events can be used as an independent probe of the cosmic SFH (e.g. Dahlen et al. 2012) or, if this is known from other estimators, constrain the stellar initial mass function along with the mass range for core collapse SN progenitor (e.g. Botticella et al. 2008). There have been claims of a mismatch between the current estimate of the SFH and the observed rate of core collapse SNe that needs to be investigated further (Horiuchi et al. 2011). A proposed explanation is that a large fraction of core collapse SNe remains hidden in particular in the very dusty nuclear regions of starburst galaxies (Mannucci et al. 2007) and correcting for these (e.g. Mattila et al. 2012) can lead to core-collapse SN rates consistent with the expectations from the cosmic SFH (Dahlen et al. 2012).

In this respect a NIR SN search with *Euclid* is attractive because of the reduced effect of dust extinction that will allow us to derive a more complete census of all types of SNe (e.g. Maiolino et al. 2002; Mannucci et al. 2003). It has been shown that the bias in observed rates due to dust extinction is expected to increase with redshift even for SNe Ia (e.g. Mannucci et al. 2007; Mattila et al. 2012 and references therein) and can be a dominant factor above $z \sim 1$.

While the most heavily extinguished SNe will remain out of reach even for *Euclid*, the DESIRE survey will allow the detection of a large population of intermediate extinction SNe which current optical searches mostly miss. All together, DESIRE will significantly increase the number of core collapse SNe in the highest redshift bins which are not well sampled now.

Finally, we stress that for the purpose of collecting transient statistics, parallel observations with the *Euclid* optical channel (VIS) would be very valuable. With the combination of IR filters and optical (unfiltered) monitoring, DESIRE will provide detections, as well as light and colour curves that can be used for the transient photometric classification and therefore extended ground based follow-up is not required for this purpose.

Aside from SNe, the DESIRE project will provide a unique database for the study of active galactic nucleus (AGN) variability. This can be used to identify AGN, in particular those of fainter magnitude that are more difficult to detect with other methods, and hence probe the evolution of the faint end of the AGN luminosity function up to high redshifts (e.g. Sarajedini et al. 2011). At the same time the data will contribute to our understanding the physics of AGN variability in the IR spectral window. It has also been proposed that the detailed AGN light curves may allow reverberation mapping measurements of AGN/QSO/SuperEddington accreting massive Balck Holes. Those are currently being studied as possible "standard candles" that could extend to larger redshifts the range provided by SNe Ia for measuring distances (e.g. Kaspi et al. 2005; Watson et al. 2011; Bentz et al. 2013; Marziani & Sulentic 2014; Wang et al. 2013a).

10.2. The DESIRE ultra deep field

By the end of the DESIRE survey, an area of 10 deg^2 will have been imaged 90 times, giving a final stacked depth of 28 to 28.5 mag (*AB*, 5 sigma point source limit) in i, z, y, J and H bands.

Such an "Ultra-deep field" would make a unique legacy, being about 2 mag deeper than the *Euclid* Deep survey (40 deg^2 reaching AB = 26) while JWST will reach deeper limits but on a much smaller area (its survey capability is constrained by NIRCAMs FoV of 2.2×4.4 arcmin^2, simultaneously observed in two bands). Examples of uses for such data include very high redshift ($z > 8$) galaxy and QSO surveys going approximately two magnitudes fainter down the luminosity function than the baseline *Euclid* Deep surveys described in Laureijs et al. (2011). We also note that the spectroscopic SNe Ia host sample that would be obtained as part of DESIRE will provide calibration of deep photometric redshifts within this ultra-deep *Euclid* field, which will be of lasting legacy value.

Although *Euclid* VIS data is not used in the SN light curve analysis (because of its broad wavelength range), the high spatial resolution imaging of VIS would be a powerful complement. If the VIS imager were allowed to integrate while the NIR DESIRE images are collected, the resulting stacked VIS image would reach $R \sim 28$ (5 sigma for an extended source of $0.3''$ *FWHM*). Such deep and sharp *Euclid* VIS images would allow deep morphological studies of galaxies in the field (for which matching depth multicolour data would also be available, see above). Using the several hundred dithered exposures of the field, the resulting stack can afford a finer pixelisation than the instrument 0.1″/pixel scale. Such a deep stack would enable measurement of the location of transients within their hosts, providing information on possible progenitor scenarios. In the case of SNe Ia, the position within the host has been found to correlate with photometric and spectroscopic properties of the SNe themselves (Wang et al. 1997; Wang et al. 2013b), which may yield further improvements on cosmological parameter constraints.

11. Summary

We have simulated a high-statistics SN Ia Hubble diagram which consists of three surveys, which in turn cover the whole redshift range from $z \sim 0$ to $z = 1.55$. The high-redshift part relies on deep NIR imaging from *Euclid* and concurrent observations in i and z bands from the ground, which consist of monitoring the same 10 deg^2 footprint for two seasons of 6 months each. During each season, *Euclid* observes the fields approximately half of the time, so the total survey time on *Euclid* amounts to 6 months (including ~40% overheads).

We have placed sufficiently stringent observing quality requirements so that all surveys are effectively redshift-limited. We have assumed that the systematic calibration uncertainties are 0.01 mag (i.e. about two times larger than current achievements), we have included a correlated irreducible distance modulus uncertainty to account for possible evolution systematics of the SN population with redshift, and accounted for both statistical and systematic uncertainties of the SN model used to fit the light curves. Despite these conservative assumptions, we find that this large scale Hubble diagram, when combined with a 1D *Planck* geometrical prior, can deliver stringent purely geometrical dark energy constraints: a static equation of state is constrained to $\sigma(w) = 0.022$. We find that the anticipated performance is fairly robust to changing the assumptions on the size of the leading systematic uncertainties. DESIRE is therefore an exciting prospect for cosmology, providing significant constraints on dark energy that are independent of *Euclid*'s other probes, while the resulting ultra-deep NIR imaging would enable a wealth of Legacy science.

Appendix A: Simulating point source photometry uncertainties

In order to simulate the precision of SN observations, we have to derive the flux measurement uncertainty from the value of the source flux, the instrument characteristics, and the observing conditions. For a point source (SNe are point sources) the expected content of a pixel p_i reads:

$$p_i = f\psi_i + (d + s)T$$

where f is the object flux, ψ_i the PSF at pixel i (i.e. the fraction of the object flux in this pixel), d is the dark current per pixel, s is the sky background per pixel per unit time, and T is the exposure time. The flux of a supernova is obtained by integrating the

(redshifted) SN spectrum in the bandpass of the instrument, accounting for the distance. Expressing all quantities in electrons, the variance reads:

$$V_i = f\psi_i + (d + s)T + r^2$$

where r is the rms read noise and the other terms are just Poisson variance. A least-squares fit of f to the image should minimise:

$$\chi^2 = \sum_i [I_i - p_i]^2 / V_i$$

where I_i are the measured pixel flux values. The flux estimator reads:

$$\hat{f} = \frac{\sum_i I_i \psi_i / V_i}{\sum_i \psi_i^2 / V_i}$$

and its variance:

$$Var(\hat{f}) = \frac{1}{\sum_i \psi_i^2 / V_i}.$$

This flux variance is statistically optimal and it is the expression we use in our simulator. How V_i depends on the object flux determines how $Var(\hat{f})$ behaves at the bright and faint ends. At large flux, $Var(\hat{f}) \rightarrow f$, as expected from Poisson statistics. Faint sources are those for which sky and dark current dominate the variance. In this regime, the pixel variance becomes stationnary ($v_i \equiv v = V_i = (d + s)T + r^2$), and the flux variance reads:

$$Var(\hat{f}) = v \frac{1}{\sum_i \psi_i^2 d}.$$

The rightmost factor has the dimension of an area (expressed in number of pixels) and is often called the noise equivalent area (NEA). It summarises the PSF quality for photometry of point sources:

$$NEA = \frac{1}{\sum_i \psi_i^2}, \tag{A.1}$$

with $\sum_i \psi_i = 1$. This expression accounts for pixelisation, and is always larger than 1 pixel. For a well sampled Gaussian, the noise equivalent area reads $4\pi\sigma^2$, where σ is expressed in pixels. The NEA values for the *Euclid* bands are provided (in arcsec^2) in Table 1. The *Euclid* NIR imager is sufficiently coarsely sampled for the NEA to vary with the source position within a pixel by 10 to 20% rms. Our simulator makes use of a single position that delivers a NEA representative of the average.

One might note that the above arguments ignore that, in PSF photometry, one usually has to fit for both position and flux. However, for an even PSF function, position and flux are uncorrelated, and fitting the position together with the flux does not degrade the flux variance.

The algebra above applies to measurements in a single image, while supernova photometry requires to subtract an image of the field without the supernova (deemed "reference image"). The impact of this subtraction is discussed in the next appendix.

Appendix B: Evaluating the influence of a finite reference image depth

The fluxes of a supernova are obtained by subtracting supernova-free images from images sampling the light curve. Since the same supernova-free image (or image set) is subtracted from all

SN epochs, the inferred supernovae fluxes are statistically correlated by the noise on these supernovae-free images, deemed reference. The SN fluxes f_i^{SN} (where i indexes epochs) can be written as:

$$f_i^{SN} = f_i - f_{ref}$$

where f_i is the flux in image i and f_{ref} is the flux measured (at the same position) on the reference image. The covariance matrix of SN fluxes reads

$$C_{ij} \equiv Cov(f_i^{SN}, f_j^{SN}) = \delta_{ij} Var(f_i) + \sigma_{ref}^2$$

with $\sigma_{ref}^2 \equiv Var(f_{ref})$. In matrix notation:

$$W \equiv C^{-1} = (D + \sigma_{ref}^2 \mathbf{1}\mathbf{1}^T)^{-1} = D^{-1} - \sigma_{ref}^2 \frac{(D^{-1}\mathbf{1})(D^{-1}\mathbf{1})^T}{1 + \sigma_{ref}^2 \mathbf{1}^T D^{-1} \mathbf{1}}$$

where $D_{ij} \equiv \delta_{ij} Var(f_i)$, $\mathbf{1}$ is just a vector filled with 1's, and we have made use of the Woodbury matrix identity. Modern differential photometry techniques (e.g. Holtzman et al. 2008) do not explicitly subtract a reference image, but instead fit a model to images both with and without the supernova, but this does not change the structure of the output SN flux covariance matrix.

The measurements f_i are used to fit the light curve parameters θ by minimising

$$\chi^2 = [A\theta - F]^T W [A\theta - F],$$

where $F \equiv (f_1^{SN}, \ldots, f_n^{SN})$ and $A\theta = E[F]$ (E[X] denotes the expectation value of the random variable X). The inverse covariance matrix of estimated parameters reads

$$C_{\hat{\theta}}^{-1} = A^T W A = \sum_i w_i h_i h_i^T - \sigma_{ref}^2 \frac{\sum_i w_i h_i \sum_i w_i h_i^T}{1 + \sigma_{ref}^2 \sum_i w_i}, \tag{B.1}$$

where h_i are the rows of A (i.e. $h_i = \partial E[f_i^{SN}]/\partial\theta$), $w_i^{-1} \equiv Var(f_i^{SN})$, and sums run over the considered measurements. We use this expression to account for finite reference depth. For an amplitude parameter a in a single band (i.e. all light curve points scale with a), we have $h_i(a) \propto E[f_i] \equiv \phi_i$, so that the variance of $\hat{a}$, with other parameters fixed, reads

$$\left[\frac{Var(\hat{a})}{a^2}\right]^{-1} = \sum_i w_i \phi_i^2 - \sigma_{ref}^2 \frac{[\sum_i w_i \phi_i]^2}{1 + \sigma_{ref}^2 \sum_i w_i},$$

where the second term is the contribution of the finite reference depth.

Appendix C: Supernovae in the *Euclid* deep field(s)

In this section we study the reach of repeated *Euclid* standard visits regarding distances to SNe Ia. In the *Euclid* wide field survey, NIR photometry is primarily aimed at securing photometric redshifts of galaxies. This is turned into the requirement $m_{AB} = 24$ point sources are measured at 5σ in each of the three NIR bands, fulfilled by the NIR photometry from a *Euclid* "standard visit" in the wide survey (Laureijs et al. 2011). The *Euclid* deep survey is constructed from repeated standard visits of the same fields, 40 visits being the baseline, both to increase depth and for calibration purposes. The latter impose that the observation sequence be exactly the same as in the wide survey.

Following the adopted way to evaluate depth for the *Euclid* wide survey, we simulated three exposures of 79, 81 and 48 s each in the y, J and H bands respectively as a "standard visit".
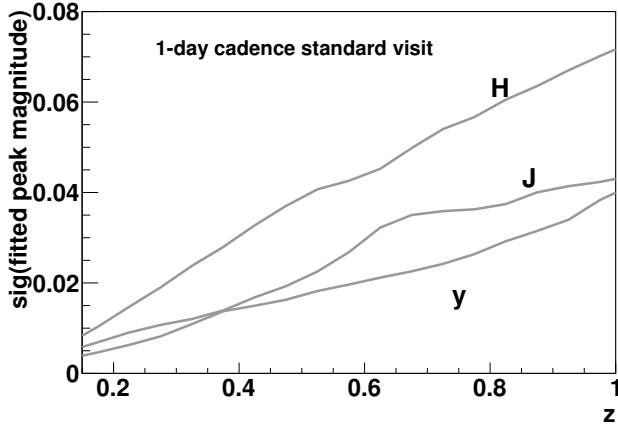
Fig. C.1. Precisions of the fitted amplitude of light curves with a one-day cadence of standard visits, as a function of redshift. The requirement of 0.04 is met at $z <\sim 1$ in y and J, and $z < 0.5$ in H.

Fig. D.1. Average peak *AB* magnitude of SNe Ia observed in the *Euclid* bands as a function of their redshift, in a flat ΛCDM model, as predicted by our SaltNIR model, trained on nearby multi-band SN Ia events from Contreras et al. (2010).

The visits indeed acquire four of these images, but the envisaged dithers between these four exposures are such that most of the covered sky area indeed only has three exposures.

We simulated supernovae observed with a one-day cadence which is probably the fastest possible cadence, and find that the precision of light curve amplitudes is below 0.04 mag up to redshifts of ~1, 0.9 and 0.5 for y, J and H respectively, as shown in Fig. C.1. Unfortunately, H being the reddest band, it is most useful at the high end of the redshift interval, as we aim at covering the same restframe spectral range at all redshifts. These SN simulations require to model SNe at wavelengths redder than what SALT2 covers and we have assembled for these simulations a SN Ia model in the NIR described in Appendix D.

This one-day cadence would allow us to survey about 10 deg^2, if exclusively observing this area, at least for some period of time. Optimistically assuming that we operate the one-day cadence over 6 months (i.e. visiting the fields 180 times rather than 40 times as currently envisioned), and integrating events up to $z = 1$ (which marginally meets our quality requirements), we would collect about 500 SN Ia events, i.e. only about what SNLS collected.

We hence believe that the *Euclid* deep fields will not deliver data that allows one to measure a compelling set of SN distances, even considering a number of visits far above the *Euclid* current plans.

Appendix D: SN Ia model in the rest-frame NIR

Since at low redshift, NIR bands address redder restframe spectral regions than those covered by SALT2, we developed a simple SN model designed to deliver realistic amplitudes and light curve shapes up to almost 2 microns in the rest frame, following the SALT model strategy Guy et al. (2005). It consists of optimising broadband corrections to an empirical spectral series in order to reproduce a set of training light curves. Our "SaltNIR" model makes use of the E. Hsiao spectral SN template (Hsiao et al. 2007), with broadband corrections derived using the first release of low-redshift events from the Carnegie Supernova Project (Contreras et al. 2010). The wavelength restframe coverage is [330, 1800] nm for the central wavelengths of the simulated filters. The training data set misses the restframe z-band which hence consists of the spectral template corrected by interpolations between i and Y bands. The peak brightnesses
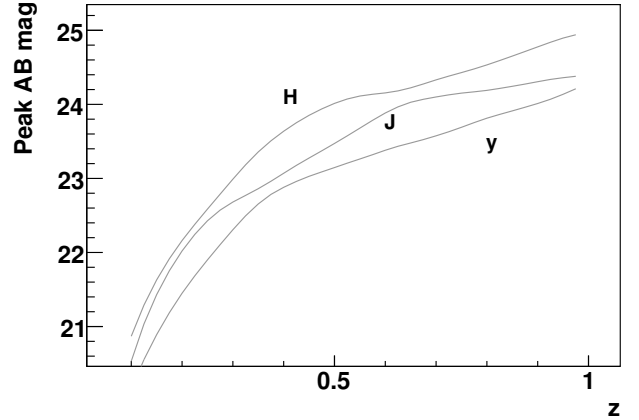
predicted by this model in *Euclid* bands are shown in Fig. D.1 and available in computer-readable form[6].

Appendix E: Material for SN-only forecasts

We here provide the distance constraints that the proposed observing sketch could deliver, including all statistical correlations. This can be combined with other probes as desired. We parametrise the distance-redshift relation as linear piecewise relation parametrised at equidistant pivot points $z_i = \delta z * i$, with $i = 0...N$. We define $d_i \equiv H_0 d_M(z_i)/c$ and linearly interpolate distance values between the pivot points. d_M refers to the proper motion distance:

$$d_M(z) = \frac{c}{H_0 \sqrt{|\Omega_k|}} \text{Sin}\left(\sqrt{|\Omega_k|} \int_0^z \frac{dz'}{H(z')} \right)$$

where $\text{Sin}(x) = \sinh(x)$, x, $\sin(x)$ according to the sign of the curvature. The d_i values define the cosmology (or more precisely the distance-redshift relation), except for the two first ones, for which we impose $d_0 = 0$ and $d_1 = \delta z$. We provide the inverse of the covariance matrix of the d_i ($i \geqslant 2$) parameters obtained from SNe alone, marginalised over all nuisance parameters.

Given an isotropic cosmological model that defines the proper motion distance $d_{mod}(z; \theta)$ as a function of some cosmological parameters θ, we define the residuals to some fiducial cosmology θ_0 as:

$$R_i = d_{mod}(z_{i+2}; \theta) - d_{mod}(z_{i+2}; \theta_0) \tag{E.1}$$

where the lowest index of R is 0. Distances should be understood here as dimensionless, i.e. $H_0 d_M/c$. The least-squares constraints expected from SNe around the θ_0 model simply read:

$$\chi^2 = R^T W R \tag{E.2}$$

where W is the matrix we provide in computer-readable format[7]. This SN χ^2 can then be added to χ^2 from other probes to obtain overall cosmology constraints.

We have checked that with $\delta z = 0.025$, the cosmological constraints (with our CMB prior) computed directly and going through this binned distance scheme agree to better than 1%. With $\delta z = 0.025$, there are 63 control points from $z = 0$ to $z = 1.55$, and we provide a matrix of dimension 61, omitting the first

---

6 http://supernovae.in2p3.fr/~astier/desire-paper/
7 http://supernovae.in2p3.fr/~astier/desire-paper/

two points as explained above. To generate this matrix, we used a flat ΛCDM model with $\Omega_M = 0.27$, but the current uncertainties of the distance-redshift relation should not require to alter this W matrix for cosmologies that yield a realistic distance-redshift relation.

References

Albrecht, A., Bernstein, G., Cahn, R., et al. 2006 [arXiv:astro-ph/0609591]
Albrecht, A., Amendola, L., Bernstein, G., et al. 2009 [arXiv:0901.0721]
Amati, L., & Valle, M. D. 2013, Int. J. Mod. Phys. D, 22, 30028
Amendola, L., Appleby, S., Bacon, D., et al. 2013, Liv. Rev. Relat., 16, 6
Astier, P., Guy, J., Regnault, N., et al. 2006, A&A, 447, 31
Astier, P., Guy, J., Pain, R., & Balland, C. 2011, A&A, 525, A7
Astier, P., El Hage, P., Guy, J., et al. 2013, A&A, 557, A55
Balland, C., Baumont, S., Basa, S., et al. 2009, A&A, 507, 85
Bazin, G., Ruhlmann-Kleider, V., Palanque-Delabrouille, N., et al. 2011, A&A, 534, A43
Bean, R., Bernat, D., Pogosian, L., Silvestri, A., & Trodden, M. 2007, Phys. Rev. D, 75, 064020
Bentz, M. C., Denney, K. D., Grier, C. J., et al. 2013, ApJ, 767, 149
Bernardeau, F., & Brax, P. 2011, J. Cosmol. Astropart. Phys., 6, 19
Bernstein, J. P., Kessler, R., Kuhlmann, S., et al. 2012, ApJ, 753, 152
Betoule, M., Marriner, J., Regnault, N., et al. 2013, A&A, 552, A124
Betoule, M., Kessler, R., Guy, J., et al. 2014, A&A, 568, A22
Blake, C., Kazin, E. A., Beutler, F., et al. 2011, MNRAS, 418, 1707
Blondin, S., Prieto, J. L., Patat, F., et al. 2009, ApJ, 693, 207
Blondin, S., Matheson, T., Kirshner, R. P., et al. 2012, AJ, 143, 126
Botticella, M. T., Riello, M., Cappellaro, E., et al. 2008, A&A, 479, 49
Boulade, O., Charlot, X., Abbon, P., et al. 2003, in Instrument Design and Performance for Optical/Infrared Ground-based Telescopes, eds. M. Iye, & A. F. M. Moorwood, Proc. SPIE, 4841, 72
Burenin, R. A., & Vikhlinin, A. A. 2012, Astron. Lett., 38, 347
Campbell, H., D'Andrea, C. B., Nichol, R. C., et al. 2013, ApJ, 763, 88
Cardelli, J. A., Clayton, G. C., & Mathis, J. S. 1989, APJ, 345, 245
Chevallier, M., & Polarski, D. 2001, Int. J. Mod. Phys. D, 10, 213
Childress, M., Aldering, G., Antilogus, P., et al. 2013, ApJ, 770, 108
Chotard, N., Gangler, E., Aldering, G., et al. 2011, A&A, 529, L4
Conley, A., Sullivan, M., Hsiao, E. Y., et al. 2008, ApJ, 681, 482
Conley, A., Guy, J., Sullivan, M., et al. 2011, ApJS, 192, 1
Contreras, C., Hamuy, M., Phillips, M. M., et al. 2010, AJ, 139, 519
Dahlen, T., Strolger, L.-G., Riess, A. G., et al. 2012, ApJ, 757, 70
D'Andrea, C. B., Gupta, R. R., Sako, M., et al. 2011, ApJ, 743, 172
Drake, A. J., Djorgovski, S. G., Mahabal, A., et al. 2012, in IAU Symp. 285, eds. E. Griffin, R. Hanisch, & R. Seaman, 306
Flaugher, B. L., Abbott, T. M. C., Annis, J., et al. 2010, in SPIE Conf. Ser., 7735
Foley, R. J., & Kasen, D. 2011, ApJ, 729, 55
Foley, R. J., & Kirshner, R. P. 2013, ApJ, 769, L1
Graur, O., & Maoz, D. 2013, MNRAS, 430, 1746
Graur, O., Poznanski, D., Maoz, D., et al. 2011, MNRAS, 417, 916
Graur, O., Rodney, S. A., Maoz, D., et al. 2014, ApJ, 783, 28
Green, J., Schechter, P., Baltay, C., et al. 2012 [arXiv:1208.4012]
Gupta, R. R., D'Andrea, C. B., Sako, M., et al. 2011, ApJ, 740, 92
Guy, J., Astier, P., Nobili, S., Regnault, N., & Pain, R. 2005, A&A, 443, 781
Guy, J., Astier, P., Baumont, S., et al. 2007, A&A, 466, 11
Guy, J., Sullivan, M., Conley, A., et al. 2010, A&A, 523, A7
Hamuy, M., & Pinto, P. A. 2002, ApJ, 566, L63
Hayden, B. T., Gupta, R. R., Garnavich, P. M., et al. 2013, ApJ, 764, 191
Hicken, M., Challis, P., Kirshner, R. P., et al. 2012, ApJS, 200, 12
Holtzman, J. A., Marriner, J., Kessler, R., et al. 2008, AJ, 136, 2306
Hook, I. M. 2013, Roy. Soc. Lond. Philosoph. Trans. Ser. A, 371, 20282
Horiuchi, S., Beacom, J. F., Kochanek, C. S., et al. 2011, ApJ, 738, 154
Howell, D. A., Sullivan, M., Perrett, K., et al. 2005, ApJ, 634, 1190
Hsiao, E. Y., Conley, A., Howell, D. A., et al. 2007, ApJ, 663, 1187
Ivezic, Z., Tyson, J. A., Acosta, E., et al. 2008 [arXiv:0805.2366]
Kaspi, S., Maoz, D., Netzer, H., et al. 2005, ApJ, 629, 61
Keller, S. C., Schmidt, B. P., Bessell, M. S., et al. 2007, PASA, 24, 1
Kelly, P. L., Hicken, M., Burke, D. L., Mandel, K. S., & Kirshner, R. P. 2010, ApJ, 715, 743
Kessler, R., Becker, A. C., Cinabro, D., et al. 2009, ApJS, 185, 32
Kessler, R., Cinabro, D., Bassett, B., et al. 2010, ApJ, 717, 40
Kessler, R., Guy, J., Marriner, J., et al. 2013, ApJ, 764, 48
Kim, A. G., & Miquel, R. 2006, Astropart. Phys., 24, 451
Lampeitl, H., Smith, M., Nichol, R. C., et al. 2010, ApJ, 722, 566
Laureijs, R., Amiaux, J., Arduini, S., et al. 2011 [arXiv:1110.3193]
Law, N. M., Kulkarni, S. R., Dekany, R. G., et al. 2009, PASP, 121, 1395
Le Fevre, O., Tasca, L. A. M., Cassata, P., et al. 2014, A&A, submitted [arXiv:1403.3938]
Leibundgut, B. 1988, Ph.D. Thesis, Univ. Basel., Switzerland
Leinert, C., Bowyer, S., Haikala, L. K., et al. 1998, A&AS, 127, 1
Lentz, E. J., Baron, E., Branch, D., Hauschildt, P. H., & Nugent, P. E. 2000, ApJ, 530, 966
Li, W., Chornock, R., Leaman, J., et al. 2011, MNRAS, 412, 1473
Lidman, C., Ruhlmann-Kleider, V., Sullivan, M., et al. 2013, PASA, 30, 1
Linder, E. V. 2003, Phys. Rev. Lett., 90, 091301
Linder, E. V. 2005, Phys. Rev. D, 72, 043529
Lue, A., Scoccimarro, R., & Starkman, G. D. 2004, Phys. Rev. D, 69, 124015
Maguire, K., Kotak, R., Smartt, S. J., et al. 2010, MNRAS, 403, L11
Maguire, K., Sullivan, M., Ellis, R. S., et al. 2012, MNRAS, 426, 2359
Maiolino, R., Vanzi, L., Mannucci, F., et al. 2002, A&A, 389, 84
Mannucci, F., Maiolino, R., Cresci, G., et al. 2003, A&A, 401, 519
Mannucci, F., Della Valle, M., Panagia, N., et al. 2005, A&A, 433, 807
Mannucci, F., Della Valle, M., & Panagia, N. 2006, MNRAS, 370, 773
Mannucci, F., Della Valle, M., & Panagia, N. 2007, MNRAS, 377, 1229
Maoz, D., & Mannucci, F. 2012, PASA, 29, 447
Maoz, D., Mannucci, F., & Brandt, T. D. 2012, MNRAS, 426, 3282
Maoz, D., Mannucci, F., & Nelemans, G. 2014, ARA&A, 52, 107
Marziani, P., & Sulentic, J. W. 2014, Adv. Space Res., 54, 1331
Mattila, S., Dahlen, T., Efstathiou, A., et al. 2012, ApJ, 756, 111
Miyazaki, S., Komiyama, Y., Nakaya, H., et al. 2012, in SPIE Conf. Ser., 8446
Mukherjee, P., Kunz, M., Parkinson, D., & Wang, Y. 2008, Phys. Rev. D, 78, 083521
Nugent, P., Sullivan, M., Ellis, R., et al. 2006, ApJ, 645, 841
Palanque-Delabrouille, N., Ruhlmann-Kleider, V., Pascal, S., et al. 2010, A&A, 514, A63
Pan, Y.-C., Sullivan, M., Maguire, K., et al. 2013, MNRAS
Peacock, J. A., Schneider, P., Efstathiou, G., et al. 2006, ESA-ESO Working Group on Fundamental Cosmology, Tech. Rep.
Perlmutter, S., Aldering, G., Goldhaber, G., et al. 1999, ApJ, 517, 565
Perrett, K., Balam, D., Sullivan, M., et al. 2010, AJ, 140, 518
Perrett, K., Sullivan, M., Conley, A., et al. 2012, AJ, 144, 59
Planck Collaboration XVI. 2014, A&A, 571, A16
Rau, A., Kulkarni, S. R., Law, N. M., et al. 2009, PASP, 121, 1334
Regnault, N., Conley, A., Guy, J., et al. 2009, A&A, 506, 999
Rest, A., Scolnic, D., Foley, R. J., et al. 2014, ApJ, 795, 44
Riess, A. G., Filippenko, A. V., Challis, P., et al. 1998, AJ, 116, 1009
Riess, A. G., Strolger, L., Tonry, J., et al. 2004, ApJ, 607, 665
Riess, A. G., Strolger, L.-G., Casertano, S., et al. 2007, ApJ, 659, 98
Riess, A. G., Macri, L., Casertano, S., et al. 2011, ApJ, 730, 119
Ripoche, P. 2008, Moriond Proceedings (Cosmology)
Rodney, S. A., Riess, A. G., Dahlen, T., et al. 2012, ApJ, 746, 5
Rodney, S. A., Riess, A. G., Strolger, L.-G., et al. 2014, AJ, 148, 13
Rubin, D., Knop, R. A., Rykoff, E., et al. 2013, ApJ, 763, 35
Sako, M., Bassett, B., Connolly, B., et al. 2011, ApJ, 738, 162
Sako, M., Bassett, B., Becker, A. C., et al. 2014, ApJS, submitted [arXiv:1401.3317]
Sarajedini, V. L., Koo, D. C., Klesman, A. J., et al. 2011, ApJ, 731, 97
Schlegel, D. J., Bebek, C., Heetderks, H., et al. 2009 [arXiv:0904.0468]
Schmidt, B. P., Suntzeff, N. B., Phillips, M. M., et al. 1998, ApJ, 507, 46
Schrabback, T., Hartlap, J., Joachimi, B., et al. 2010, A&A, 516, A63
Scolnic, D., Rest, A., Riess, A., et al. 2014a, ApJ, 795, 45
Scolnic, D. M., Riess, A. G., Foley, R. J., et al. 2014b, ApJ, 780, 37
Silverman, J. M., Foley, R. J., Filippenko, A. V., et al. 2012, MNRAS, 425, 1789
Smith, M., Nichol, R. C., Dilday, B., et al. 2012, ApJ, 755, 61
Spergel, D., Gehrels, N., Breckinridge, J., et al. 2013 [arXiv:1305.5422]
Stritzinger, M. D., Phillips, M. M., Boldt, L. N., et al. 2011, AJ, 142, 156
Sullivan, M., Le Borgne, D., Pritchet, C. J., et al. 2006, ApJ, 648, 868
Sullivan, M., Conley, A., Howell, D. A., et al. 2010, MNRAS, 406, 782
Sullivan, M., Guy, J., Conley, A., et al. 2011, ApJ, 737, 102
Suzuki, N., Rubin, D., Lidman, C., et al. 2012, ApJ, 746, 85
Tripp, R., & Branch, D. 1999, ApJ, 525, 209
Walker, E. S., Hachinger, S., Mazzali, P. A., et al. 2012, MNRAS, 427, 103
Wang, L., Hoeflich, P., & Wheeler, J. C. 1997, ApJ, 483, L29
Wang, X., Filippenko, A. V., Ganeshalingam, M., et al. 2009, ApJ, 699, L139
Wang, J.-M., Du, P., Valls-Gabaud, D., Hu, C., & Netzer, H. 2013a, Phys. Rev. Lett., 110, 081301
Wang, X., Wang, L., Filippenko, A. V., Zhang, T., & Zhao, X. 2013b, Science, 340, 170
Watson, D., Denney, K. D., Vestergaard, M., & Davis, T. M. 2011, ApJ, 740, L49
Wood-Vasey, W. M., Miknaitis, G., Stubbs, C. W., et al. 2007, ApJ, 666, 694
Zheng, C., Romani, R. W., Sako, M., et al. 2008, AJ, 135, 1766